Title
The Effects of Downward Longwave Radiation on Low-Level Clouds: An Observational Analysis

Author
Macpherson, Christopher Colin

Publication Date
2024

Peer reviewed|Thesis/dissertation

UNIVERSITY OF CALIFORNIA SAN DIEGO

The Effects of Downward Longwave Radiation on Low-Level Clouds: An Observational Analysis

A dissertation submitted in partial satisfaction of the requirements for the degree Doctor of Philosophy

in

Earth Sciences

by

Christopher Colin Macpherson

Committee in charge:

Professor Joel Norris, Chair
Professor Jennifer Burney
Professor Amato Evan
Professor Jan Kleissl

2024

The dissertation of Christopher Colin Macpherson is approved, and it is acceptable in quality and form for publication on microfilm and electronically.

University of California San Diego

2024

TABLE OF CONTENTS

LIST OF ABBREVIATIONS

LW↓	downward longwave radiation
TOA	top-of-atmosphere
CRE	cloud radiative effect
SWCRE	shortwave cloud radiative effect
LWCRE	longwave cloud radiative effect
NETCRE	net cloud radiative effect
CO_2	carbon dioxide
ΔLW↓	instantaneous radiative forcing from a quadrupling of carbon dioxide
f	low-level cloud fraction
LWP	liquid water path
z_{ct}	low-level cloud-top height
α_{cld}	cloud albedo
ε_{cld}	cloud longwave emissivity
ΔSWCRE	change in shortwave cloud radiative effect due to a perturbation in downward longwave radiation
ΔLWCRE	change in longwave cloud radiative effect due to a perturbation in downward longwave radiation
ΔNETCRE	change in net cloud radiative effect due to a perturbation in downward longwave radiation
CCCM	NASA A-Train Integrated CALIPSO, CloudSat, CERES, and

	MODIS (CCCM) dataset
CERES	NASA Clouds and the Earth's Radiant Energy System
f_{upper}	cloud fraction of clouds above 3000 m
FBCT	NASA CERES Flux by Cloud Type dataset
CCF	cloud-controlling factor
ω_{700hPa}	vertical pressure velocity at 700 hPa
WS	low-level wind speed
Tadv	low-level atmospheric temperature advection
RH_{3000m}	relative humidity at 3000 m
SST	sea surface temperature
EIS	estimated inversion strength

LIST OF FIGURES

LIST OF TABLES

ACKNOWLEDGEMENTS

First, I would like to thank my wife, Lindsay, for her constant patience and unwavering support. Not once did she doubt my abilities during this process, and I will forever be in her debt for the sacrifices she made to help me reach this goal. Thank you to my mom, dad, and sister for teaching me to follow my dreams when I was a child and then helping me achieve them. I also want to acknowledge my four-legged "lab assistants," Ernie, Linus, and Penny for their emotional support. Lastly, I want to thank my advisor, Joel Norris. I remember meeting with Joel as a prospective student and discussing low-level clouds in his office. Little did I know that meeting would completely change my life. I cannot thank him enough for his guidance, wisdom, and faith in my abilities. The work in this document was supported by the Future Investigators in NASA Earth and Space Science and Technology research grant number 80NSSC20K160.

Chapters one, two, and three contain material currently being prepared for submission for publication. Christopher Macpherson; and Norris, Joel. "The Effects of Downward Longwave Radiation on Low-Level Clouds: A Regional Analysis". The dissertation author was the primary investigator and author of this paper. Chapters four, five, and six contain material currently being prepared for submission for publication. Christopher Macpherson; and Norris, Joel. "The Effects of Downward Longwave Radiation on Low-Level Clouds: A Global Analysis". The dissertation author was the primary investigator and author of this paper.

VITA

2012 Bachelor of Science, Michigan State University

2021 Master of Science, University of California San Diego

2024 Doctor of Philosophy, University of California San Diego

FIELDS OF STUDY

Major Field: Earth Sciences

Studies in Climate Science
Professor Joel Norris

ABSTRACT OF THE DISSERTATION

The Effects of Downward Longwave Radiation on Low-Level Clouds: An Observational Analysis

by

Christopher Colin Macpherson

Doctor of Philosophy in Earth Sciences

University of California San Diego, 2024

Professor Joel Norris, Chair

Low-level marine clouds are abundant over the global ocean and are an important element of Earth’s energy budget. They are sensitive to numerous meteorological variables, including downward longwave radiation, a parameter that has received little attention in observational studies. Using satellite observations and reanalysis data, we show that enhanced downward longwave radiation reduces low-level marine cloud fraction, liquid water path, and cloud-top height. The relationships between low-level cloud properties and downward longwave radiation are isolated from the effects of other cloud-controlling factors through both a compositing and multiple linear regression analysis. These relationships are quantified for clouds over the eastern subtropical oceans and used to calculate the radiative adjustment due to a perturbation in downward longwave radiation under the radiative forcing from 4xCO_2. Both methods achieve comparable results. The study area is then expanded to the global ocean from 60° N to 60° S, and another multiple linear regression analysis is performed. Owing to reductions in cloud fraction, liquid water path, and cloud-top height, both the shortwave and longwave cloud radiative effects are weakened globally by 5.5 % and 6.5 %, respectively. This reduces the net cloud radiative effect of low-level clouds by approximately 0.5 Wm^{-2} or 5.3 %. The relative importance of downward longwave radiation as a cloud-controlling factor is also examined. Low-level cloud fraction and liquid water path are influenced more by a typical 16-day anomaly in downward longwave radiation than any other cloud-controlling factor. Downward longwave radiation also exhibits confounding effects on estimated inversion strength and the relative humidity above the cloud top by weakening the influence of these cloud-controlling factors on low-level cloud properties. These results provide observational evidence that downward longwave radiation substantially impacts low-level cloud properties.

Chapter 1 Executive Introduction

1.1 Introduction

Clouds play an important role in Earth's energy budget because they reflect shortwave radiation while also absorbing and emitting longwave radiation. The reflection of shortwave radiation provides a cooling effect on the Earth, while the absorption and emission of longwave radiation provide a warming effect. Low-level marine clouds reflect a large amount of shortwave radiation back to space because of their large cloud fraction and amount of liquid water. They also emit a sizable amount of longwave radiation because they have warm cloud-top temperatures and large amounts of liquid water. The combination of strong shortwave reflection and strong longwave emission to space creates a large net cooling effect (Hartmann et al. 1992) that, along with their coverage over more than 20% of the world's oceans (Eastman et al. 2011), makes low-level clouds an important regulator of Earth's temperature. Low-level marine clouds are sensitive to changing meteorological conditions, and understanding how they respond to global warming has been a critical area of study (Schneider 1972; Arking 1991; Norris et al. 2016; Scott et al. 2020) since even small changes in low-level marine clouds can have large impacts on Earth's energy budget (Slingo 1990).

Over the eastern subtropical oceans, the marine boundary layer is contained between a cool sea surface and a strong atmospheric temperature inversion. These meteorological conditions facilitate the growth of optically thick, low-level marine clouds, primarily stratocumulus (Wood 2012). Along with sea surface temperature and the atmospheric temperature inversion, other meteorological parameters that influence low-level clouds, called cloud-controlling factors, have been identified. These include the relative humidity of the atmosphere above the cloud tops, vertical pressure velocity above the cloud tops, near-surface wind speed, and near-surface temperature advection. Numerous studies, both observational and modeling, have measured the influence of these cloud-controlling factors on low-level clouds (Stevens and Brenguier 2009; Klein et al. 2017; Scott et al. 2020; among others). A cooler sea surface temperature increases low-level cloudiness by reduced entrainment evaporation because there is a decrease in the humidity difference between the surface and the top of the marine boundary layer (Bretherton et al. 2013; Bretherton and Blossey 2014). A stronger boundary layer temperature inversion reduces the entrainment of dry air from the free troposphere, which increases low-level cloudiness (Wood and Bretherton 2006; Myers and Norris 2013). Greater free-tropospheric humidity reduces entrainment drying, leading to more low-level cloudiness (Van Der Dussen et al. 2015; Myers and Norris 2016; Eastman and Wood 2018). A weakening in subsidence relative to the entrainment rate leads to increased cloud height (Myers and Norris 2013). Increased low-level wind speed and cold temperature advection destabilize the lower boundary layer, leading to more convection and low-level cloudiness (Brueck et al. 2015; Scott et al. 2020). Lastly, a more emissive free troposphere from increased CO_2, water vapor, or upper-level clouds reduces low-level cloudiness by suppressing cloud-top radiative cooling (Bretherton et al. 2013; Schneider et al. 2019). Although downward longwave radiation has been identified as influencing low-level cloudiness (Klein et al. 2017), only a few observational studies have been conducted to examine its relative strength as a cloud-controlling factor (Christensen et al. 2013; Eastman and Wood 2018; Jian et al. 2022).

Beyond the eastern subtropical oceans, stratocumulus clouds are found across the global ocean, especially in the midlatitudes (Klein and Hartmann 1993; Norris and Klein 2000). Midlatitude stratocumulus clouds develop under different circumstances than those in the eastern subtropical oceans (Wood 2012), however, they are still primarily maintained through cloud-top radiative cooling. The other low-level cloud type frequent over the ocean is cumulus, often found in the tropics and subtropics (Warren et al. 1988; Norris 1998). Convection is the primary driver in cumulus development (Stommel 1947; Malkus 1954; Emanuel 1991). However, radiative cooling enhances convection within a cumulus cloud (Guan et al. 1997; Klinger et al. 2017). For this reason, we suspect that cumulus clouds may be sensitive to changes in downward longwave radiation.

Studies have examined the response of low-level clouds to global warming from increased CO_2 in both large-eddy simulations and global circulation models (Zelinka et al. 2012; Blossey et al. 2013). These studies found that with increasing sea surface temperatures, low-level cloud fraction and liquid water amounts decrease, reducing the amount of shortwave radiation that low-level clouds reflect. However, in addition to responding to changes in sea surface temperature from rising CO_2, low-level clouds also respond directly to changes in CO_2. As CO_2 in the atmosphere increases, downward longwave radiation reaching the boundary layer comes from lower, warmer regions of the free troposphere. This increases longwave radiation reaching low-level cloud tops and decreases radiative cooling (Chen and Cotton 1987). As radiative cooling is a major factor in generating turbulent mixing that connects the cloud to the moisture at the ocean's surface (Lilly 1968), this decrease in radiative cooling lowers cloud fraction and thickness (Bretherton et al. 2013; Schneider et al. 2019). A smaller cloud fraction decreases the reflection of shortwave radiation because the cloud is less horizontally extensive. Additionally, reducing cloud fraction increases the amount of emitted longwave radiation reaching the top of the atmosphere because the cloud absorbs less longwave radiation from the surface. A thinner cloud, or one with a lower liquid water content, decreases the reflection of shortwave radiation because the cloud has a lower albedo. Also, a thinner cloud may transmit more longwave radiation emitted by the surface, thus increasing the amount of longwave radiation reaching the top of the atmosphere. The third effect a decrease in turbulent mixing can have on low-level clouds is a reduction in cloud-top height. A lower cloud-top height emits more longwave radiation because it is warmer. When these effects are combined, there is a net increase in radiative flux on the Earth (Zelinka et al. 2013) because the increase in longwave emission is less than the decrease in shortwave reflection. Clouds can make this adjustment on time scales of days to weeks, long before the sea surface temperatures adjust to changes in CO_2 (Cao et al. 2012; Kamae and Watanabe 2012).

While simulations have been used to investigate low-level clouds, they are not perfect representations of natural conditions. Large-eddy simulations must parameterize the large-scale dynamics that control extensive areas of low-level clouds (Blossey et al. 2013), while global models are limited by their large horizontal resolution, which cannot resolve the small-scale processes controlling low-level clouds. Nonetheless, simulations have been used to quantify the impact of changes in CO_2 on low-level clouds because there is no exact observational equivalent since variations in CO_2 on the time scales of months to decades are much smaller than a doubling of carbon dioxide. However, unlike CO_2, water vapor and upper-level clouds do vary greatly on short time scales of hours to days, and have a considerable effect on downward longwave radiation, so their radiative impact can be used as a proxy for that of CO_2. One observational study found that upper-level clouds increase downward longwave radiation reaching low-level cloud tops and reduce radiative cooling by approximately 20% (Christensen et al. 2013). The same study also found that the reduction in cloud-top radiative cooling led to lower cloud-top heights and reduced liquid water amounts at night through a reduction in turbulent mixing. However, the impact that these changes have on the radiative properties of low-level clouds has not yet been observationally documented.

1.2 Introduction to the Dissertation

In this study, we use satellite observations to quantify the effects of downward longwave radiation on low-level marine clouds' radiative properties. We observe how variations in downward longwave radiation caused by upper-level clouds and water vapor affect low-level cloud fraction, liquid water path, and cloud-top height. Once these relationships are quantified, we estimate the change in the reflection of shortwave radiation and the absorption and emission of longwave radiation by low-level clouds. To conclude, we determine the influence of downward longwave radiation as an independent cloud-controlling factor on cloud properties.

The datasets we use contain the vertical profile of clouds and radiative flux, allowing us to obtain low-level cloud properties even while upper-level clouds are overhead and downward longwave radiation at the top of the boundary layer. One challenge of observational studies is that it is difficult to isolate downward longwave radiation's impact on low-level clouds because both longwave radiation and clouds are affected by meteorological processes.

We address this limitation using two methods applied to three 20° latitude by 20° longitude regions in the eastern subtropical oceans. The first method identifies the cloud-controlling factors correlated with low-level cloud fraction, liquid water path, and cloud-top height. We then hold these cloud-controlling factors constant through a data binning process to isolate the relationship between low-level cloud properties and downward longwave radiation. In the second method, we use a multiple linear regression analysis that computes regression coefficients representing the cloud property relationship with downward longwave radiation independent of variations in other parameters. We then estimate the change in the cloud radiative effect due to changes in cloud properties from the perturbation in downward longwave perturbation associated with a quadrupling of CO_2. We compare the results of the two methods to determine if the multiple linear regression analysis is suitable for application over a larger area. Furthermore, we standardize cloud and meteorological data to rank the influence of downward longwave radiation on cloud properties.

We then expand the study area to encompass the global ocean, from 60° N to 60° S, and separate the area into different regimes based on the climatology of particular cloud-controlling factors. As this is a significantly larger area, we forgo the compositing method and only use the multiple linear regression analysis to quantify the relationships between downward longwave radiation and low-level clouds. Similar to the approach taken with the regional study, we see how variations in cloud properties due to a perturbation in downward longwave radiation impact the cloud radiative effect. Lastly, we standardize cloud and meteorological data to rank the influence of cloud-controlling factors on cloud properties. Lastly, we determine the strength of downward longwave radiation as a cloud-controlling factor and identify any confounding effects it has on other cloud-controlling factors. In doing so, we find observational equivalents to modeling studies.

Acknowledgments

Chapter 1 contains material currently being prepared for submission for publication. Christopher Macpherson; and Norris, Joel. “The Effects of Downward Longwave Radiation on Low-Level Clouds: A Regional Analysis”. The dissertation author was the primary investigator and author of this paper.

Chapter 2 Data and Methods

2.1. Determining cloud radiative effects

Following prior studies, we quantify the low-level cloud radiative response to changes in downward longwave radiation (LW↓) in terms of the top-of-atmosphere (TOA) cloud radiative effect (CRE). The cloud radiative effect consists of both shortwave (SWCRE) and longwave (LWCRE) components, the sum of which produces the net cloud radiative effect (NETCRE). The impact LW↓ has on low-level cloud properties is expressed using a perturbation expansion that consists of the mean state of each cloud property and its response to a perturbation in LW↓. The cloud properties we investigate are cloud fraction, albedo, emissivity, and cloud-top height. We select these four cloud properties because they dominate the radiative response of low-level clouds.

We begin by defining SWCRE as

$$SWCRE = SW_{clr} - SW_{all} \qquad (1)$$

Where SW_{clr} is the SW radiative flux measured at the TOA under clear-sky conditions and SW_{all} is the SW radiative flux at the TOA under all-sky conditions. SW_{all} can be represented as

$$SW_{all} = (1 - f)SW_{clr} + fSW_{cld} \qquad (2)$$

where f is the low-level cloud fraction and SW_{cld} is the SW radiative flux at the TOA from the part of the area covered by low-level clouds. Substituting this definition of SW_{all} into equation 1 produces

$$SWCRE = f(SW_{clr} - SW_{cld}) \qquad (3)$$

The SW radiative fluxes in equation 3 are the product of solar insolation and the albedo of the area, and substituting for these relationships yields

$$SWCRE = fS_o(\alpha_{clr} - \alpha_{cld}) \qquad (4)$$

where S_o is the solar insolation measured at the TOA, α_{clr} is the albedo of the clear part of the area, and α_{cld} is the albedo of the part of the area covered by low-level clouds. A quadrupling of CO_2 ($4xCO_2$) will produce a positive downward perturbation in LW↓ reaching low-level clouds, which we define as ΔLW↓. Expanding equation 4 to represent the first-order response in f and α_{cld} to perturbations in LW↓ yields

$$\Delta SWCRE = \overline{S_0}(\overline{\alpha_{clr}} - \overline{\alpha_{cld}})(\partial f/\partial LW\downarrow)\Delta LW\downarrow \quad - \overline{S_o f}(\partial \alpha_{cld}/\partial LW\downarrow)\Delta LW\downarrow \qquad (5)$$

where ΔSWCRE is the change in SWCRE arising from the low-level cloud response to a perturbation in LW↓. An overline denotes the mean value for a parameter. We define ($\partial f/\partial$LW↓) as the low-level cloud fraction response to changes in LW↓ and ($\partial\alpha_{cld}$ /∂LW↓) as the albedo response of the cloud-covered area to changes in LW↓ and then multiply each term by the perturbation ΔLW↓. Reducing low-level cloud fraction due to enhanced LW↓ reduces SWCRE, as there is less cloud to reflect SW radiative flux to space. Reducing low-level cloud albedo from enhanced LW↓ reduces SWCRE since the cloud reflects less SW radiative flux. We do not consider a perturbation in α_{clr} because it does not arise from a change in low-level cloud properties.

We define LWCRE as

$$LWCRE = LW_{clr} - LW_{all} \qquad (6)$$

where LW_{clr} is the LW radiative flux at the TOA for clear-sky conditions and LW_{all} is the LW radiative flux for all-sky conditions. Similar to the derivation for SWCRE, LW_{all} can be broken down into

$$LW_{all} = (1 - f)LW_{clr} + fLW_{cld} \qquad (7)$$

where LW_{cld} is the LW radiative flux from the part of the area covered by low-level clouds. Substituting this expression for LW_{all} into equation 6 yields

$$LWCRE = f(LW_{clr} - LW_{cld}) \qquad (8)$$

Next, we describe LW radiative flux emitted by the surface (B_s) and decompose LW_{clr} and LW_{cld} into

$$B_s = \epsilon_s \sigma T_s^4 \qquad (9)$$

$$LW_{clr} = B_s g_{clr} \qquad (10)$$

$$LW_{cld} = \epsilon_s B_s g_{cld} \qquad (11)$$

where g_{clr} is the ratio of LW radiative flux at the TOA compared to the LW radiative flux emitted by the surface for the clear part of the area, g_{cld} is the ratio of LW radiative flux at the TOA compared to the LW radiative flux emitted by the surface for the part of the area covered by low-level clouds, ε_s is the LW emissivity of the surface, σ is the Stefan-Boltzmann constant, and T_s is the sea surface temperature. Substituting B_s, g_{clr}, and g_{cld} into equation 8 yields

$$LWCRE = B_s f (g_{clr} - g_{cld}) \qquad (12)$$

In the cloud-free parts of the area, there is LW radiative flux emission from the surface, the boundary layer, and the free troposphere. The part of the area covered by low-level clouds complicates the situation further, as there is LW radiative flux emission from clouds, the surface, the boundary layer, and the free troposphere. Additionally, the LW radiative flux emitted by low-level clouds is not the same as the amount at the TOA, as there is absorption and emission in the free troposphere. Therefore, we introduce a new term, g_{free}, which represents the ratio of LW radiative flux at the TOA to LW radiative flux emitted by opaque low-level clouds. The LW radiative flux emitted at the cloud top as if it were a blackbody is B_{ct} and T_{ct} is the cloud-top temperature.

$$g_{free} = LW_{cld} / B_{ct} \qquad (13)$$

$$B_{ct} = \sigma T_{ct}^4 \qquad (14)$$

For non-opaque low-level clouds, we redefine LW_{cld} as

$$LW_{cld} = g_{free}\epsilon_{cld}B_{ct} + (1 - \epsilon_{cld})\, LW_{clr} \qquad (13)$$

where ε_{cld} is low-level cloud emissivity. The term $(1 - \varepsilon_{cld})LW_{clr}$ is the LW radiative flux at the TOA transmitted through the low-level clouds and otherwise the same as the LW radiative flux in the clear part of the area. We substitute g_{free} for the cloud-covered part of the area into equation 12.

$$LWCRE = f\epsilon_{cld}B_s[\epsilon_s g_{clr} - g_{free}(B_{ct}/B_s)] \qquad (15)$$

Equation 15 allows us to compute LWCRE in terms of low-level cloud fraction and emissivity but not changes in cloud-top height. We take cloud-top height into account because a lower cloud top is warmer and will emit more LW radiation. Therefore, it is useful to relate cloud-top temperature to sea surface temperature. We define cloud-top temperature as

$$T_{ct} = T_s - \Gamma z_{ct} \qquad (16)$$

where Γ is the lapse rate and z_{ct} is the cloud-top height. We then calculate the ratio of cloud-top blackbody emission to surface blackbody emission as

$$B_{ct}/B_s = (T_s - \Gamma z_{ct})^4/T_s^4 \qquad (17)$$

and approximate it to the first order as

$$B_{ct}/B_s = 1 - 4\Gamma z_{ct}/T_s \qquad (18)$$

Substituting equation 18 into equation 15 yields

$$LWCRE = f\epsilon B_s[\epsilon_s g_{clr} - g_{free}(1 - 4\Gamma z_{ct}/T_s)] \qquad (19)$$

Expanding equation 19 to represent first-order changes in f, ε_{cld}, and z_{ct} brought about by ΔLW↓ yields

$$\begin{aligned}\Delta LWCRE = {} & \overline{\varepsilon_{cld}B_s}[\overline{\varepsilon_s g_{clr}} - \overline{g_{free}}(1 - 4\overline{\Gamma z_{ct}}/\overline{T_s})](\partial f/\partial LW{\downarrow})\Delta LW{\downarrow} \\ & + \overline{fB_s}[\overline{\varepsilon_s g_{clr}} - \overline{g_{free}}(1 - 4\overline{\Gamma z_{ct}}/\overline{T_s})](\partial \varepsilon_{cld}/\partial LW{\downarrow})\Delta LW{\downarrow} \\ & + 4\overline{f\varepsilon_{cld}B_s g_{free}\Gamma}/\overline{T_s}\,(\partial z_{ct}/\partial LW{\downarrow})\Delta LW{\downarrow} \qquad (20)\end{aligned}$$

where ($\partial f/\partial$LW↓) is the cloud fraction response to changes in LW↓, ($\partial \varepsilon_{cld}/\partial$LW↓) is the cloud emissivity response to changes in LW↓ and ($\partial z_{ct}/\partial$LW↓) is the cloud-top height response to changes in LW↓. These low-level cloud responses are multiplied by the perturbation ΔLW↓. A reduction in cloud emissivity due to enhanced LW↓ reduces LWCRE, as does a decrease in low-level cloud fraction because more LW radiative flux emitted by the surface can reach the TOA compared to LW radiative flux emitted by low-level clouds. Lastly, a lower cloud-top height due to enhanced LW↓ will further decrease LWCRE because the temperature difference between the cloud-top and the surface is smaller, and the cloud will emit more LW radiative flux. Changes related to B_s, g_{clr}, g_{free}, Γ, and SST are not considered since they do not stem from changes in low-level cloud properties.

Combining ΔSWCRE with ΔLWCRE gives ΔNETCRE as

$$\Delta NETCRE = \Delta SWCRE + \Delta LWCRE \qquad (21)$$

Note that the previous equations were derived assuming that no upper-level clouds were present because the radiative effect of low-level clouds is difficult to calculate when they are under upper-level clouds. For this reason, we consider low-level CRE changes in the area not covered by upper-level clouds and scale ΔSWCRE, ΔLWCRE, and ΔNETCRE by the fraction of the area not covered by upper-level clouds.

2.2. The CALIPSO, CloudSat, CERES, and MODIS dataset

The principal dataset used in this study is the National Aeronautics and Space Administration (NASA) A-Train Integrated CALIPSO, CloudSat, CERES, and MODIS (CCCM) dataset version RelB1. We use this dataset for detailed vertical profiles of clouds, radiative flux, temperature, and pressure. A significant strength of this dataset is the ability to discern individual cloud layers within a multilayer cloud scene. The Cloud Profiling Radar instrument on CloudSat and the Cloud-Aerosol Lidar with Orthogonal Polarization instrument on CALIPSO are active sensing instruments that can observe low-level clouds beneath upper-level clouds even within the same vertical profile. Additionally, the CCCM dataset provides vertical irradiance profiles computed using a radiative transfer model with cloud properties derived from the CCCM sensors.

While most CCCM data is organized at the CERES footprint level, CCCM cloud data is organized at a more detailed sub-footprint level. Each CERES footprint may contain up to 16 cloud groups with differing cloud fractions, and each cloud group includes up to 6 vertical cloud layers, all containing the same horizontal cloud fraction. We process these cloud groups and layers to create singular values for low-level cloud-top height and cloud fraction for each CERES footprint. We begin by setting a limit of 3000 m above sea level as the maximum possible top of the boundary layer. This upper limit was found to be approximately the minima in vertical cloud fraction and approximately corresponds to the 700 hPa height level. An average is calculated for the footprint cloud-top height (z_{ct}) from all cloud groups containing a cloud layer below 3000 m, weighted by cloud group fraction, using only the first cloud layer with a cloud-top height below 3000 m. As clouds can have bases below 3000 m, they can occur alongside low-level clouds. This reduces low-level cloud fraction by limiting the footprint area available for low-level clouds. Therefore, we calculate the low-level cloud fraction as the sum of all cloud group fractions with cloud tops below 3000 m divided by the fraction of the footprint not covered by clouds extending across 3000 m. Upper-level cloud fraction (f_{upper}) is calculated by summing all cloud group fractions that contain cloud layers with cloud base heights above 3000 m.

The CCCM LW downward flux profile estimates the instantaneous LW↓ at 3000 m, corresponding with the maximum possible top of the boundary layer. A fixed height value is used because the actual top of the boundary layer is not determined in this flux profile with sufficient vertical accuracy. The enhanced LW↓ flux profile, obtained from CCCM, is calculated using MODIS, CALIPSO, and CloudSat cloud observations and the enhanced CERES cloud algorithm (Kato et al. 2011). We exclude daytime observations to isolate the effect of LW↓ and avoid the complicating effect of solar heating on low-level clouds (Christensen et al. 2013).

Cloud radiative effect calculations require low-level cloud albedo and cloud emissivity, which are not available from the CCCM dataset. As an alternative, we estimate cloud albedo and emissivity from CCCM measurements of liquid water path (LWP) using a method that will be explained in the next section. We do not use LWP derived from MODIS because nighttime retrievals are inaccurate for clouds with large optical depths (Minnis et al. 2011). Instead, we integrate CloudSat liquid water content from the surface to 3000 m for each CCCM CERES footprint profile to obtain boundary layer LWP. Since CloudSat liquid water content is reported as the average for the portion of the CERES footprint covered by clouds occurring at any level, LWP for low-level clouds can be underestimated since areas with clouds above 3000 m but zero liquid water below 3000 m are implicitly included in the liquid water content average for levels below 3000 m. We adjust for this by multiplying the surface to 3000 m integrated liquid water content by the ratio of all-level cloud fraction to low-level cloud fraction and thereby find the LWP for low-level clouds.

2.3. CERES and Reanalysis Datasets

In addition to CCCM, we use the CERES Flux by Cloud Type (FBCT) and SYN1deg datasets. The FBCT Day_Ed4A Version 1 provides daily mean, 1° × 1° cloud properties and radiative flux observations at the TOA. This dataset uses Moderate Resolution Imaging Spectroradiometer (MODIS) radiances originating from different cloud-top pressures and optical thicknesses. It converts them into a radiative flux using the CERES angular directional model (Sun et al. 2022). We use these radiative fluxes to obtain observations of upward LW radiative flux that originates from low-level clouds (LW_{cld}) and reaches the TOA. Furthermore, the FBCT dataset also provides observations of low-level cloud-top temperature, cloud infrared emissivity, and cloud albedo, where low-level clouds are defined as those with cloud-top pressures greater than 680hPa.

The CERES SYN1deg Ed4A dataset is used for daily mean, 1° × 1° clear-sky SW (SW_{clr}) and clear-sky LW (LW_{clr}) radiative fluxes at the TOA because the CERES FBCT dataset has difficulty determining clear-sky radiative fluxes when the observed area is nearly or entirely cloud-covered. These radiative fluxes are computed with clouds removed. We also use the NASA SSF - Level 2 dataset for LW surface emissivity (ε_s) with a value of 0.982 for all locations and times (Wielicki et al. 1996).

We use Modern Era Retrospective-analysis for Research and Application Version 2 (MERRA-2) M2T3NVASM data for cloud-controlling factors (CCFs) not provided by CCCM or FBCT. This data product contains wind speed at 985 hPa, atmospheric temperature at 985 hPa, and vertical pressure velocity at 700 hPa (ω_{700hPa}). Wind speed and atmospheric temperature are needed to calculate low-level wind speed (WS) and low-level temperature advection (Tadv). MERRA-2 M2T3NVASM has a 0.5° x 0.67° spatial resolution and is available in 3-hourly time averages. These parameters are spatially averaged and temporally interpolated to align with CCCM CERES footprints. The other CCFs obtained from the CCCM dataset are relative humidity (RH_{3000m}) at 3000 m, skin temperature, which we refer to as sea surface temperature (SST) hereafter, and estimated inversion stability (Wood and Bretherton 2006), which we refer to as estimated inversion strength (EIS). The relative humidity at 3000 m is calculated from the CCCM water vapor mixing ratio, temperature, and atmospheric pressure at 3000 m.

Instantaneous observations from CCCM are not on a regular latitude-longitude grid but instead consist of continuous "tracks" of CERES footprints across the Earth. The tracks are separated by approximately 1.5° longitude and repeat every 16 days over the same track location. We align the gridded CERES datasets to CCCM CERES footprints by locating the four nearest CERES 1° × 1° values to each CCCM CERES footprint. This is repeated the day before and after the CCCM nighttime observation. These nearest location parameters are spatially averaged and temporally interpolated to the CERES footprint observation location and time. Spatial interpolation is not utilized due to occasional missing FBCT flux data for individual pressure and optical thickness bins. Cloud data from CERES FBCT contains radiative fluxes and cloud-top temperatures for two cloud-top pressure intervals and six optical depth intervals. We first find the average, weighted by cloud fraction, of the FBCT parameters for each cloud-top pressure and optical depth interval. Once completed, we then average the four CERES FBCT cloud data values, weighted by cloud fraction, to achieve a single value matched to the CCCM CERES footprint.

After aligning all data to CCCM CERES footprint locations, we determine the decorrelation scale of low-level cloud properties is a distance of about 5° latitude. This scale is needed because CCCM observations are recorded along a continuous track, and consecutive observations of low-level clouds with the same properties may be recorded. We use this decorrelation scale to average data along the same CCCM CERES footprint track into 5°-latitude intervals and then deseasonalize the data. As each CERES footprint repeats over the same location every 16 days, we calculate the seasonal cycle using a fast Fournier transform based on the 16-day repeats. We take the difference between the constructed seasonal cycle and the observations to calculate deseasonalized anomalies.

We estimate low-level cloud albedo and infrared emissivity from CCCM LWP to calculate the change in radiative properties of low-level clouds due to perturbations in LW↓. Since both cloud albedo and cloud emissivity increase with the amount of liquid water contained in clouds, variations in LWP result in a corresponding change in cloud albedo and emissivity. We use linear regression analysis in three areas of the eastern subtropical oceans to determine the relationships between deseasonalized CCCM daytime LWP anomalies and

FBCT cloud albedo anomalies as well as between deseasonalized daytime CCCM LWP anomalies and FBCT infrared emissivity anomalies. We find that the relationships between desasonalized CCCM LWP anomalies and the desasonalized FBCT cloud parameter anomalies are near linear. The resulting regression coefficients are then used to convert nighttime desasonalized CCCM LWP anomalies to desasonalized cloud albedo (α_{cld}) and cloud infrared emissivity (ε_{cld}) anomalies.

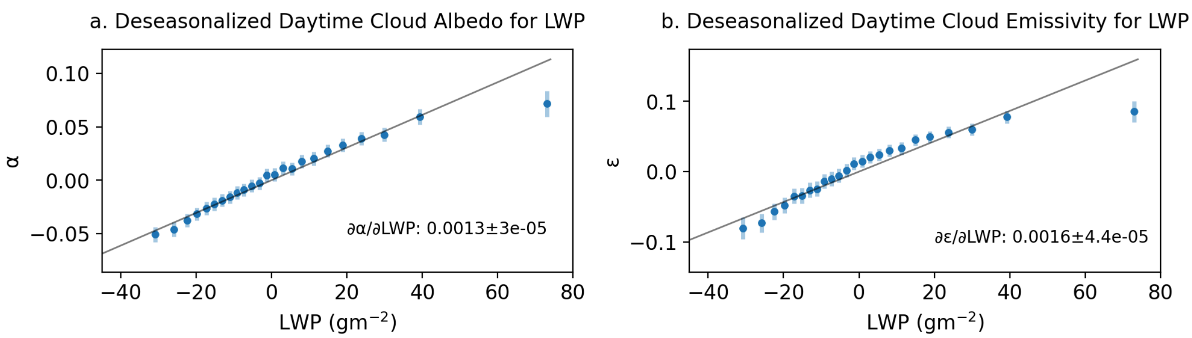

Figure 2.1: Relationship between daytime low-level cloud (a) albedo anomalies from FBCT and LWP anomalies from CCCM and (b) cloud emissivity anomalies from FBCT and LWP anomalies from CCCM. A linear regression is calculated for both relationships.

The parameters needed for the CRE perturbation equations require the combination of variables from the datasets described above. We use SW_{clr} from SYN1deg and divide it by solar insolation (S_o) from FBCT to obtain clear-sky albedo (α_{clr}). Surface LW radiative flux (B_s) is calculated from skin temperature from CCCM. Cloud-top LW radiative flux (B_{ct}) is calculated from FBCT cloud effective temperature. The cloud effective temperature is the temperature of the radiative center of cloud. The equation for g_{clr} consists of LW_{clr} from SYN1deg and the computed B_s. Also, g_{free} is derived from LW_{cld} from FBCT, the derived ε_{cld} from CCCM LWP, LW_{clr} from SYN1deg, and the computed B_{ct}. Lastly, the atmospheric lapse rate (Γ) is computed from FBCT T_{ct}, CCCM z_{ct}, and CCCM skin temperature.

2.4. Data processing

We analyze data from January 2007 to December 2010 for three regions of study: the Northeast Pacific (NEP) (120° - 140° W and 15° - 35° N), the Southeast Pacific (SEP) (75° - 95° W and 10° - 30° S), and the Southeast Atlantic (SEA) (10°E - 10° W and 10° - 30° S). Low-level clouds, particularly stratocumulus, are prevalent in these regions throughout the year (Hahn and Warren 2007; Muhlbauer et al. 2014). Cloud data in the northeastern 5° square in the South Pacific region is removed since it is mostly over land.

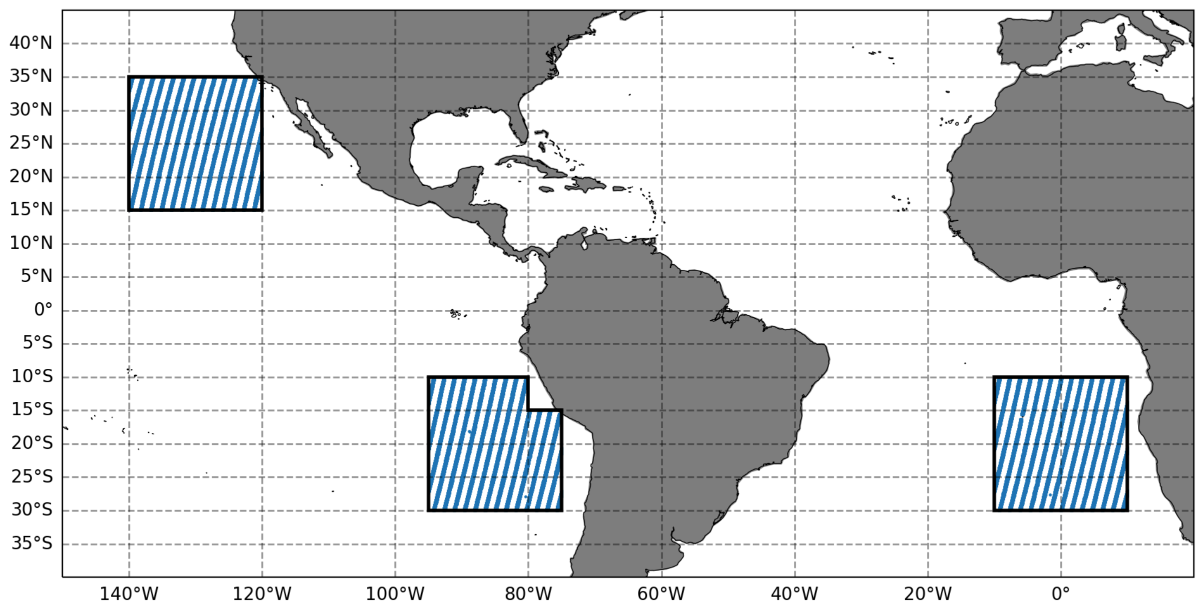

Figure 2.2: The three areas used for the regional study.

Even though data along the CERES track is averaged to 5° latitude, it may still be correlated to adjacent tracks to the east and west and to the previous observations at the same location 16 days prior due to the regional scale and persistence of meteorological conditions. To address the spatial correlation between CCCM tracks, we find the effective spatial sample size by calculating the spatial degrees of freedom according to the method outlined by

Bretherton et al. (1999) to the 5°-latitude track averages. We account for the smaller true sample size by multiplying each total uncertainty by the square root of the ratio of 5°-latitude intervals to the calculated spatial degrees of freedom, resulting in values of 2.0 for *f*, 2.4 for LWP, and 2.1 for z_{ct}. To address the temporal correlation between each 16-day repeat, we adjust the effective temporal sample size by identifying when the lag between autocorrelation values becomes negative, resulting in values of 1.2 for *f*, 1.3 for LWP, and 1.3 for z_{ct}.

Acknowledgments

Chapter 2 contains material currently being prepared for submission for publication. Christopher Macpherson; and Norris, Joel. “The Effects of Downward Longwave Radiation on Low-Level Clouds: A Regional Analysis”. The dissertation author was the primary investigator and author of this paper.

Chapter 3 Results of the Regional Study

3.1 Low-level cloud climatology and relationships with cloud-controlling factors

The climatological values of low-level cloud properties, CCFs, and CREs for the three regions are displayed in Table 3.1. Low-level cloud properties exhibit uniformity across all regions, characterized by a mean cloud fraction above 70 %, a mean liquid water path of approximately 50 gm^{-2}, and cloud-top heights ranging from about 1320 m to 1510 m. Mean CCFs also show consistency across the three regions with cool SSTs, strong subsidence, a dry above-cloud layer, a strong temperature inversion, cool low-level temperature advection, and moderate low-level wind speeds. Overall, CCF values are consistent with previous literature (Myers and Norris 2016; Scott et al. 2020) in depicting the meteorological conditions under which stratocumulus and cumulous clouds exist in the subtropical eastern oceans. Additionally, low-level clouds display strongly negative SWCRE and moderately positive LWCRE, resulting in negative NETCRE values, as expected in regions where marine stratocumulus are commonly found.

Table 3.1: Climatological means for low-level cloud properties, cloud-controlling factors, and cloud radiative effects weighted by area. Values are averages of the 5° latitude x 6.2° longitude grid boxes located within each region. Uncertainty is expressed by 95% confidence intervals.

	NEP	SEP	SEA
f (%)	74.6 ± 3.0	83.0 ± 3.8	76.0 ± 3.2
LWP (gm^{-2})	49.2 ± 4.2	53.1 ± 5.6	46.3 ± 4.2
z_{ct} (m)	1320 ± 107	1510 ± 73	1351 ± 102
LW↓ (Wm^{-2})	226 ± 6	211 ± 6	222 ± 6
SST (K)	294 ± 2	294 ± 1	295 ± 1
ω_{700hPa} (hPa day^{-1})	30.0 ± 2.9	29.1 ± 7.0	24.7 ± 3.3
RH_{3000m} (%)	29.4 ± 2.7	17.1 ± 3.1	26.7 ± 3.8
EIS (K)	4.03 ± 1.19	5.97 ± 1.09	4.13 ± 0.70
Tadv (K day^{-1})	-1.68 ± 0.20	-1.38 ± 0.19	-1.49 ± 0.28
WS (ms^{-1})	6.86 ± 0.40	7.54 ± 0.40	7.11 ± 0.36
SWCRE (Wm^{-2})	-42.3 ± 3.7	-60.3 ± 5.5	-50.5 ± 4.5
LWCRE (Wm^{-2})	8.9 ± 0.8	12.0 ± 0.9	9.3 ± 0.9
NETCRE (Wm^{-2})	-33.4 ± 3.1	-48.4 ± 4.9	-41.3 ± 4.3

In Table 3.2, we explore the correlation coefficients between low-level cloud properties and established cloud-controlling factors (Qu et al. 2014; Bretherton 2015; Klein et al. 2017; Scott et al. 2020) to gain general insight into the relatedness between these parameters. We also include LW↓ with low-level cloud properties to examine its association with the other cloud-controlling factors. The analysis reveals negative correlations between f, LWP, and z_{ct}

with LW↓, showing that negative LW↓ anomalies coincide with positive f, LWP, and z_{ct} anomalies. A stronger temperature inversion, higher wind speed, cool SST, cold temperature advection, and low relative humidity above the cloud layer correlate with a larger cloud fraction and liquid water path. A weaker temperature inversion, warm SST, cold temperature advection, strong wind speed, and low and low relative humidity above the cloud correlate with an elevated cloud-top height. Downward longwave radiation is strongly correlated with RH_{3000m}, suggesting that greater humidity levels lead to more emission of LW↓.

Table 3.2: Correlation coefficients for cloud-top height, cloud fraction, liquid water path, and downward longwave radiation at 3000 m, along with estimated inversion strength, sea surface temperature, low-level temperature advection, low-level wind speed, subsidence, and relative humidity.

	LW↓	EIS	SST	Tadv	WS	ω_{700hPa}	RH_{3000m}
f	-0.22	0.24	-0.13	-0.17	0.16	-0.01	-0.23
LWP	-0.25	0.16	-0.06	-0.07	0.03	0	-0.20
z_{ct}	-0.15	-0.32	0.05	-0.08	0.17	-0.04	-0.06
LW↓	1.00	0.08	0.01	0.13	-0.05	-0.19	0.61

3.2. The response of cloud properties to changes in LW↓

To calculate the low-level cloud response to perturbations in LW↓, we employ cloud-controlling analyses (Klein et al. 2017; Scott et al. 2020) that express changes in low-level cloud properties using a first-order Taylor series expansion in CCFs. We first implement a compositing approach to isolate the effect of LW↓ on low-level cloud properties. Deseasonalized data is organized into 1°C SST x 0.2°C EIS bins because these CCFs are correlated with cloud properties (Table 2). Within each bin, LW↓, RH_{3000m}, z_{ct}, f, and LWP anomalies are calculated and then unbinned. The z_{ct}, f, and LWP anomalies are then sorted into bins of 5% RH_{3000m} and 5 Wm^{-2} LW↓ anomalies. This allows for separating the effects of RH_{3000m} and LW↓ on low-level cloud properties. For each RH_{3000m} and LW↓ bin, we calculate the mean z_{ct}, f, and LWP anomaly. Lastly, we calculate the mean cloud property anomaly across all LW↓ bins for 5% RH_{3000m} anomaly intervals and subtract this value from the cloud property mean in each LW↓ bin. This process results in the relationship for each cloud property with LW↓ when RH_{3000m}, SST, and EIS are held constant. This step is repeated to keep LW↓ anomaly intervals constant and allow RH_{3000m} anomalies to vary.

In keeping with the correlation coefficient (r = 0.61), a positive relationship between RH_{3000m} and LW↓ is observed in Figure 3.1, which shows fraction, liquid water path, and cloud-top height anomalies as functions of LW↓ anomalies when RH_{3000m} anomaly intervals are held constant. Looking across rows of RH_{3000m} anomaly intervals, Figure 3a reveals a shift from positive to negative fraction anomalies as LW↓ anomalies shift from negative to positive. Likewise, Figure 3.1b depicts a shift from positive to negative LWP anomalies as LW↓ anomalies shift from negative to positive. No discernable relationship exists for z_{ct} anomalies with LW↓ (Fig. 3.1c). Figure 3.2 displays fraction, liquid water path, and cloud-top height anomalies as functions of RH_{3000m} anomalies when LW↓ anomaly intervals are held constant. No relationship is seen for fraction and LWP anomalies with RH_{3000m}, but z_{ct} decreases with positive RH_{3000m} anomalies. Viewing columns of LW↓ constant anomaly intervals suggests that cloud-top height anomalies shift from positive to negative as relative humidity anomalies shift from negative to positive. This indicates that humid free tropospheric air is linked with lower cloud-top heights, in consensus with Eastman and Wood (2018).

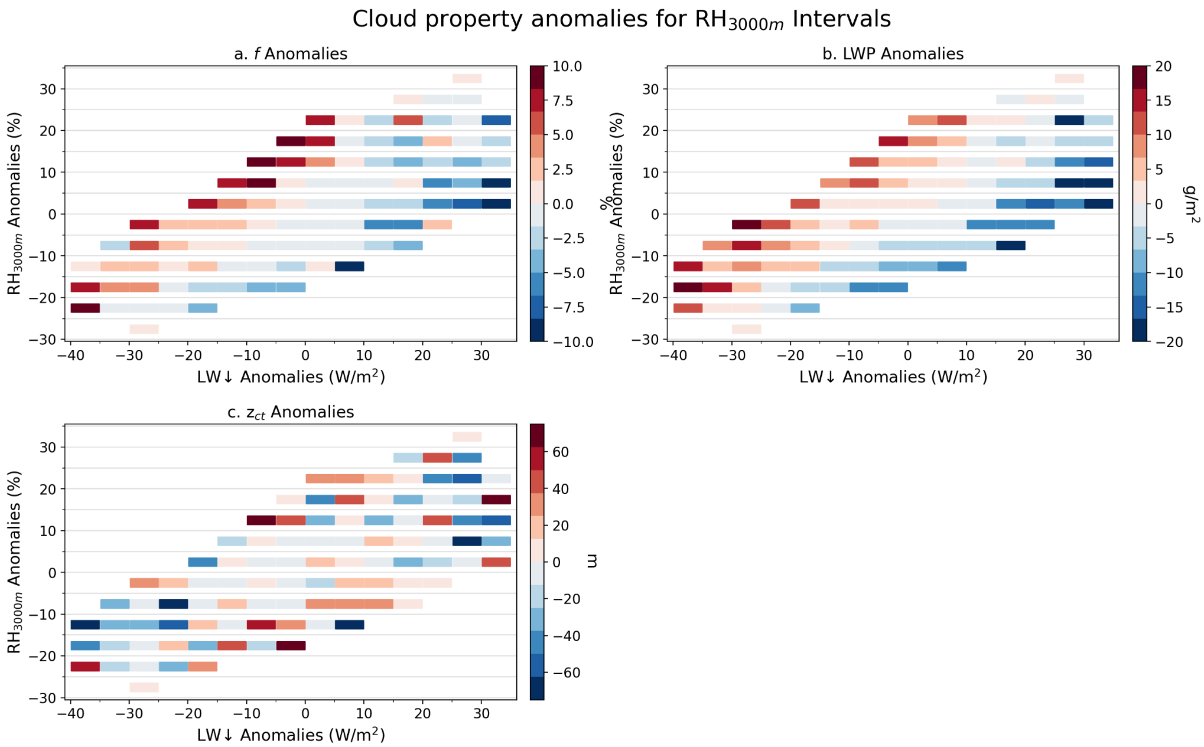

Figure 3.1: Compositing results of (a) cloud fraction anomalies, (b) liquid water path anomalies, and (c) cloud-top height anomalies with LW↓ anomalies for RH_{3000m} anomaly intervals.

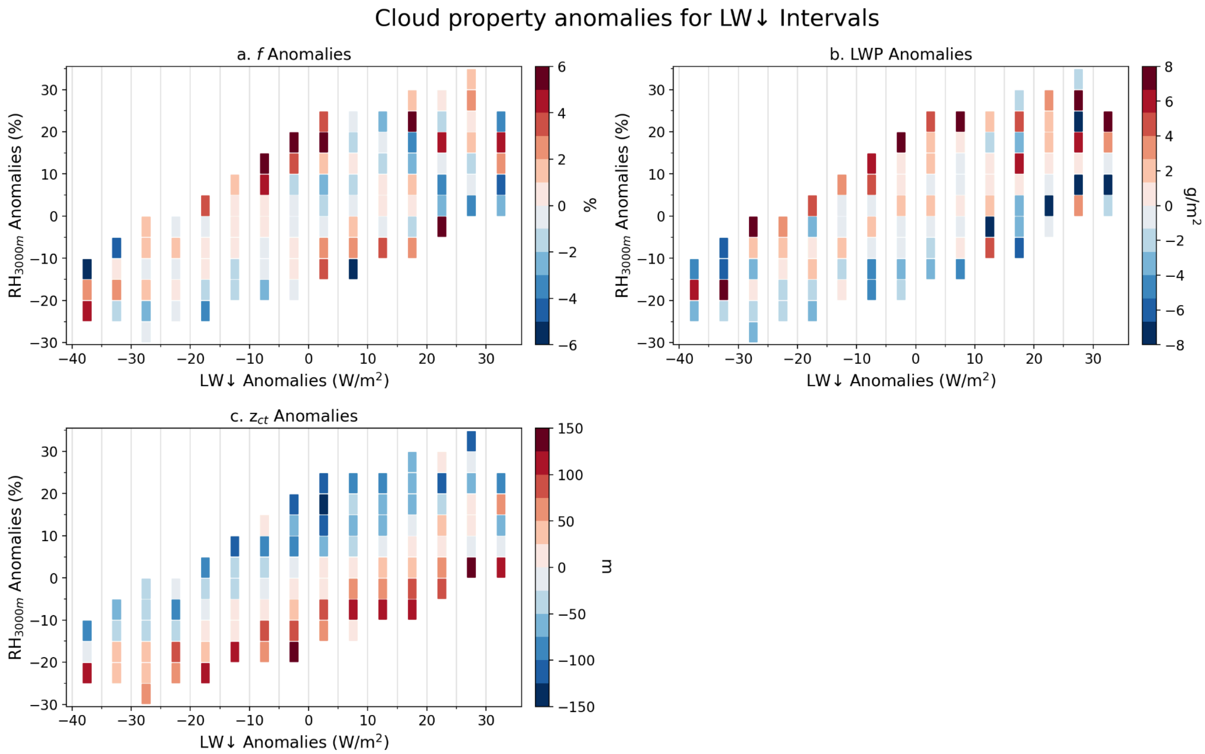

Figure 3.2: The same as Figure 3.1 but with RH_{3000m} anomalies for LW↓ anomaly intervals.

Within each 5% RH_{3000m} anomaly range, the ratio of the difference between cloud property anomalies to the difference between LW↓ anomalies is calculated for all possible pairings. The median value of all ratio differences from all RH_{3000m} anomaly ranges and weighted by average cloud fraction is the cloud property response to a change in LW↓. Uncertainty of the response is the difference between the lower 2.5% and upper 97.5% ratios divided by the square root of the total number of observations.

Along with the compositing method, we use multiple linear regression to produce regression coefficients with LW↓ using deseasonalized cloud properties and CCFs. We utilize dependent cloud properties f, LWP, and z_{ct} along with independent CCFs LW↓, RH_{3000m}, SST, EIS, Tadv, WS, and ω_{700hPa}. This method allows us to quantify the response to changes in cloud properties with LW↓, independent of all other CCFs. We calculate 95% confidence intervals for the multiple linear regression coefficients between each cloud property and LW↓ according to the Student's *t* distribution. Additionally, we calculate variance inflation factors to test for multicollinearity. Variable Inflation factors are low (<3), indicating that the seven CCFs are not highly correlated with one another. The responses of cloud properties to perturbations in LW↓, using both methods, are displayed in Table 3.3. The two methods agree that cloud fraction decreases with increasing LW↓ when other CCFs are constant. Similarly, both methods agree that LWP decreases with increasing LW↓. Lastly, both methods agree that cloud-top height may increase with LW↓. However, the results of both methods are not significant at a 95% confidence level.

Table 3.3: Low-level cloud property response to perturbations in LW↓ for the compositing and multiple linear regression methods.

Method	$\partial f/\partial$LW↓ (%/Wm^{-2})	∂LWP/∂LW↓ (gm^{-2}/Wm^{-2})	$\partial z_{ct}/\partial$LW↓ (m/Wm^{-2})
Composite	-0.23 ± 0.11	-0.52 ± 0.19	0.47 ± 1.75
Multiple Linear Regression	-0.28 ± 0.05	-0.58 ± 0.08	0.18 ± 0.71

To examine the relationships between LW↓ and low-level cloud properties more deeply, we have divided the study regions into 5° latitude x 6.2° longitude grid boxes, each containing approximately 350 data points, and applied multilinear regression. Variance inflation factors are calculated for each grid box to test for multicollinearity. We find that variable Inflation factors are low (<5) for all grid boxes. The resulting cloud property regression coefficients with LW↓ are displayed in Figure 3.3. Cloud fraction regression coefficients with LW↓ are negative for nearly all grid boxes (Fig. 3.3a), indicating widespread reductions in cloud fraction with LW↓. All three regions contain grid boxes with statistically significant regression coefficients. The strongest $\partial f/\partial$LW↓ coefficients are found in the Northeast Pacific region. Liquid water path regression coefficients with LW↓ are negative for all grid boxes (Fig. 3.3b). Most grid boxes in the NEP are statistically significant, demonstrating widespread LWP reduction with LW↓. While the mean value regression coefficient for cloud-top height with LW↓ is slightly positive (Table 3.3), approximately half of the grid boxes exhibit a negative relationship between z_{ct} and LW↓.

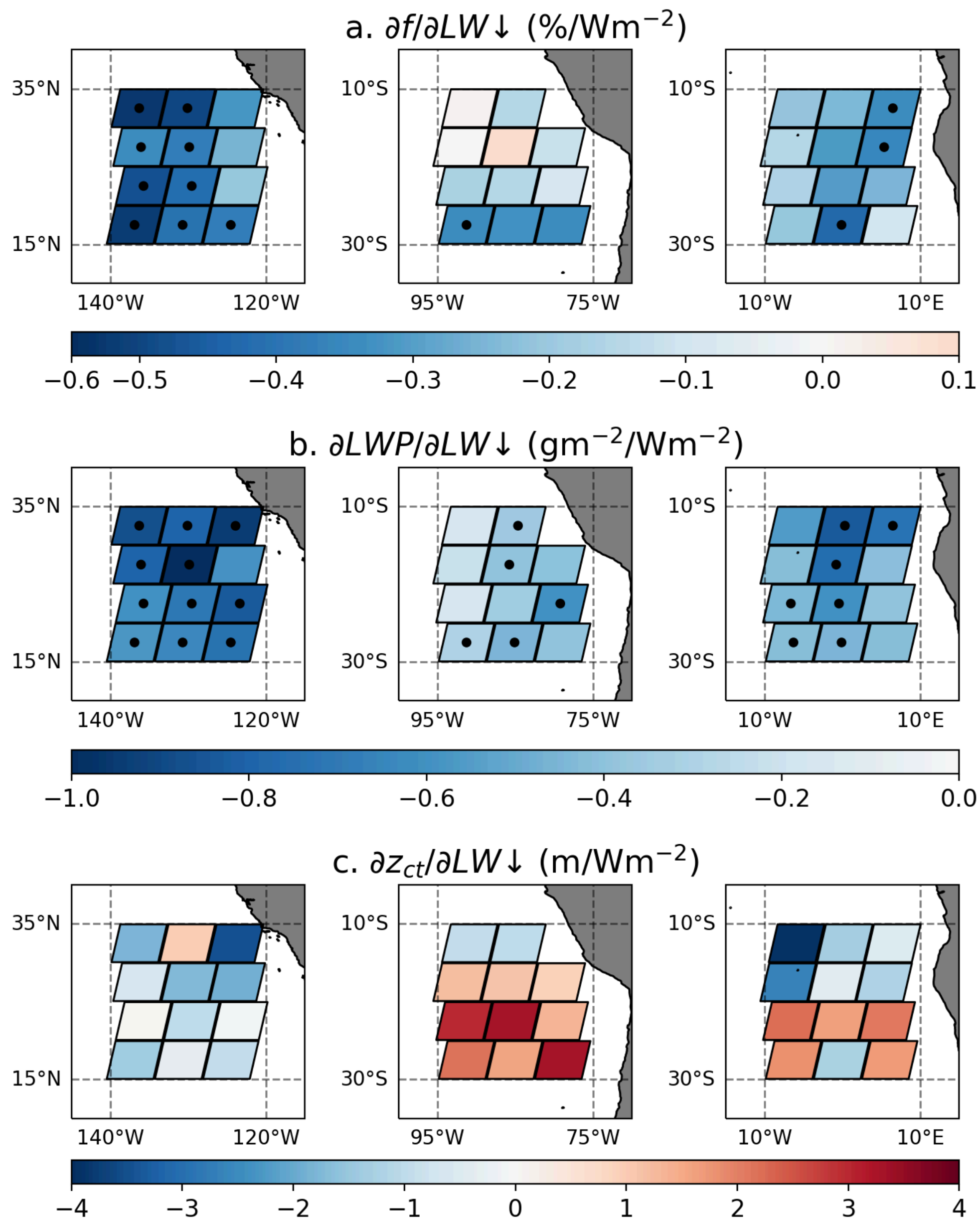

Figure 3.3: The response of low-level (a) cloud fraction, (b) liquid water path, and (c) cloud-top height to perturbations in LW↓. Multilinear regression coefficients are calculated for each 5° latitude x 6.2° longitude grid box, and stippling denotes statistically significant values. Blue values indicate negative low-level cloud property changes with increased LW↓, and red values indicate positive changes. Grid boxes are parallelogram-shaped because the CCCM tracks span the regions of study in lines from NNE to SSW.

3.3. Changes in cloud radiative effect due to changes in LW↓

The relationships $\partial f/\partial$LW↓, ∂LWP/∂LW↓, $\partial z_{ct}/\partial$LW↓, $\partial \alpha_{cld}/\partial$LW↓, and $\partial \varepsilon_{cld}/\partial$LW↓ (of which α_{cld} and ε_{cld} are derived from LWP) calculated by both methods are inputted into the CRE equations defined in section two. We then scale the CRE equations by a 7.2 Wm^{-2} perturbation in LW↓, which is representative of the radiative forcing from an instantaneous quadrupling of CO_2 (Zhang and Huang 2014).

To handle the combination of regression coefficient uncertainties, we calculate a total combined uncertainty as follows

$$\sqrt{a^2 + b^2 + 2r_{ab}ab} \qquad (22)$$

where a and b are the uncertainties of two different cloud property regression coefficients and r_{ab} is the correlation coefficient between the two cloud properties. Additionally, because there is uncertainty in the scaling to $\partial \alpha_{cld}/\partial$LW↓ and $\partial \varepsilon_{cld}/\partial$LW↓ from $\partial \alpha_{cld}/\partial$LWP and $\partial \varepsilon_{cld}/\partial$LWP, we calculate the uncertainty for $\partial \varepsilon_{cld}/\partial$LW↓ as

$$\sqrt{\left(\frac{\partial \varepsilon_{cld}}{\partial LWP}\right)_u^2 \left(\frac{\partial LWP}{\partial LW\downarrow}\right)^2 + \left(\frac{\partial LWP}{\partial LW\downarrow}\right)_u^2 \left(\frac{\partial \varepsilon_{cld}}{\partial LWP}\right)^2 + 2r_{\varepsilon_{cld}LWP}\left(\frac{\partial \varepsilon_{cld}}{\partial LWP}\right)_u \left(\frac{\partial LWP}{\partial LW\downarrow}\right)\left(\frac{\partial LWP}{\partial LW\downarrow}\right)_u \left(\frac{\partial \varepsilon_{cld}}{\partial LWP}\right)} \qquad (23)$$

and $\partial \alpha_{cld}/\partial$LW↓ as

$$\sqrt{\left(\frac{\partial \alpha_{cld}}{\partial LWP}\right)_u^2 \left(\frac{\partial LWP}{\partial LW\downarrow}\right)^2 + \left(\frac{\partial LWP}{\partial LW\downarrow}\right)_u^2 \left(\frac{\partial \alpha_{cld}}{\partial LWP}\right)^2 + 2r_{\alpha_{cld}LWP}\left(\frac{\partial \alpha_{cld}}{\partial LWP}\right)_u \left(\frac{\partial LWP}{\partial LW\downarrow}\right)\left(\frac{\partial LWP}{\partial LW\downarrow}\right)_u \left(\frac{\partial \alpha_{cld}}{\partial LWP}\right)} \qquad (24)$$

where $(\partial \varepsilon_{cld}/\partial \mathrm{LWP})_u$ is the uncertainty of the regression coefficient between cloud emissivity and liquid water path, $(\partial \alpha_{cld}/\partial \mathrm{LWP})_u$ is the uncertainty of the regression coefficient between cloud albedo and liquid water path, $(\partial LWP/\partial LW\downarrow)_u$ is the uncertainty of the regression coefficient between liquid water path and downward longwave radiation, $2r_{\varepsilon cldLWP}$ is the correlation coefficient between cloud emissivity and liquid water path, and $2_{r\alpha cldLWP}$ is the correlation coefficient between cloud albedo and liquid water path.

As described in section two, ΔSWCRE is the sum of low-level cloud changes in f ($\Delta SWCRE_{\Delta f}$) and α_{cld} ($\Delta SWCRE_{\Delta\alpha cld}$), whereas ΔLWCRE is the sum of changes in f ($\Delta LWCRE_{\Delta f}$), ε_{cld} ($\Delta LWCRE_{\Delta\varepsilon cld}$), and z_{ct} ($\Delta LWCRE_{\Delta zct}$). These changes in cloud radiative effects are displayed in Table 3.4. Following conventional sign notation for CRE, a positive value for ΔSWCRE weakens SWCRE, whereas a negative value for ΔLWCRE weakens LWCRE. Both methods produce similar results for all CRE calculations. A weakening by approximately 1 Wm^{-2} is found for $\Delta SWCRE_{\Delta f}$. This weakening is due to less cloud area to reflect incoming shortwave radiation. Due to a lower cloud albedo with increased LW↓, $\Delta SWCRE_{\Delta\alpha cld}$ is weakened. When $\Delta SWCRE_{\Delta f}$ and $\Delta SWCRE_{\Delta\alpha cld}$ are summed, we find that ΔSWCRE is greater than 2 Wm^{-2}, representing a 4.5 % reduction in climatological SWCRE. We find $\Delta LWCRE_{\Delta f}$ is weakened by approximately -0.21 $Wm^{-2,}$ and $\Delta LWCRE_{\Delta\varepsilon cld}$ is weakened by approximately -0.07 Wm^{-2}. A less emissive cloud makes the cloud-covered LW effect more similar to the clear-sky LW effect, reducing LWCRE. Lastly, positive values for $\Delta LWCRE_{\Delta zct}$ are not significant. Overall, ΔLWCRE is approximately -0.23 Wm^{-2} or a 2.3 % reduction in climatological LWCRE. Combining ΔSWCRE and ΔLWCRE leads to a change in NETCRE by about 2 Wm^{-2} for the radiative forcing under $4xCO_2$. Compared to the climatological value for NETCRE, ΔNETCRE represents a 5% reduction.

Table 3.4: Cloud radiative effect changes due to perturbations in LW↓ from the radiative forcing of an instantaneous increase in $4xCO_2$ are calculated from the relationships determined by the compositing method and the multiple linear regression method. Uncertainty is expressed by 95% confidence intervals.

	Composite	Multiple Linear Regression
$\Delta SWCRE_{\Delta f}$ (Wm^{-2})	1.04 ± 0.52	1.03 ± 0.18
$\Delta SWCRE_{\Delta \alpha cld}$ (Wm^{-2})	1.14 ± 0.41	1.28 ± 0.16
$\Delta LWCRE_{\Delta f}$ (Wm^{-2})	-0.22 ± 0.11	-0.21 ± 0.04
$\Delta LWCRE_{\Delta \varepsilon cld}$ (Wm^{-2})	-0.07 ± 0.02	-0.08 ± 0.01
$\Delta LWCRE_{\Delta zct}$ (Wm^{-2})	0.07 ± 0.26	0.03 ± 0.11
ΔSWCRE (Wm^{-2})	2.19 ± 0.77	2.31 ± 0.36
ΔLWCRE (Wm^{-2})	-0.22 ± 0.30	-0.26 ± 0.12
ΔNETCRE (Wm^{-2})	1.97 ± 0.96	2.05 ± 0.36

We also calculate ΔSWCRE, ΔLWCRE, and ΔNETCRE for each 5° latitude x 6.2° longitude grid box, the results of which are depicted in Figure 3.4. Contributions to ΔSWCRE from $\Delta SWCRE_{\Delta f}$ are positive for nearly all grid boxes, mirroring the response shown in Figure 3.4a because a negative $\partial f/\partial LW\downarrow$ results in positive $\Delta SWCRE_{\Delta f}$. Statistically significant $\Delta SWCRE_{\Delta f}$ values are found in all three regions, and the few negative $\Delta SWCRE_{\Delta f}$ values are found in the South Pacific. Values for $\Delta SWCRE_{\Delta \alpha cld}$ are positive for all grid boxes, demonstrating that the changes in α_{cld} that weaken SWCRE are common. Additionally, the magnitudes of $\Delta SWCRE_{\Delta \alpha cld}$ and $\Delta SWCRE_{\Delta f}$ are comparable for most grid boxes, indicating that both contribute similarly to ΔSWCRE. Changes in $\Delta LWCRE_{\Delta f}$ and $\Delta LWCRE_{\Delta \varepsilon cld}$ are negative for nearly all grid boxes, with changes in cloud emissivity providing much smaller contributions to ΔLWCRE than changes in cloud fraction. The cloud-top height component of ΔLWCRE is highly variable, as shown in Figure 3.4e, ranging from -0.6 Wm^{-2} to 0.6 Wm^{-2}. Positive values for $\Delta LWCRE_{\Delta z ct}$ come from increases in z_{ct} with LW↓, as a higher cloud-top height is typically colder, increasing the difference between the cloud-covered area and the clear-sky area of that grid box. The change in NETCRE is shown in Figure 3.4f, where values are positive for all grid boxes, reaching a maximum in the boxes where $\Delta SWCRE_{\Delta f}$ and $\Delta SWCRE_{\Delta \alpha cld}$ are the strongest.

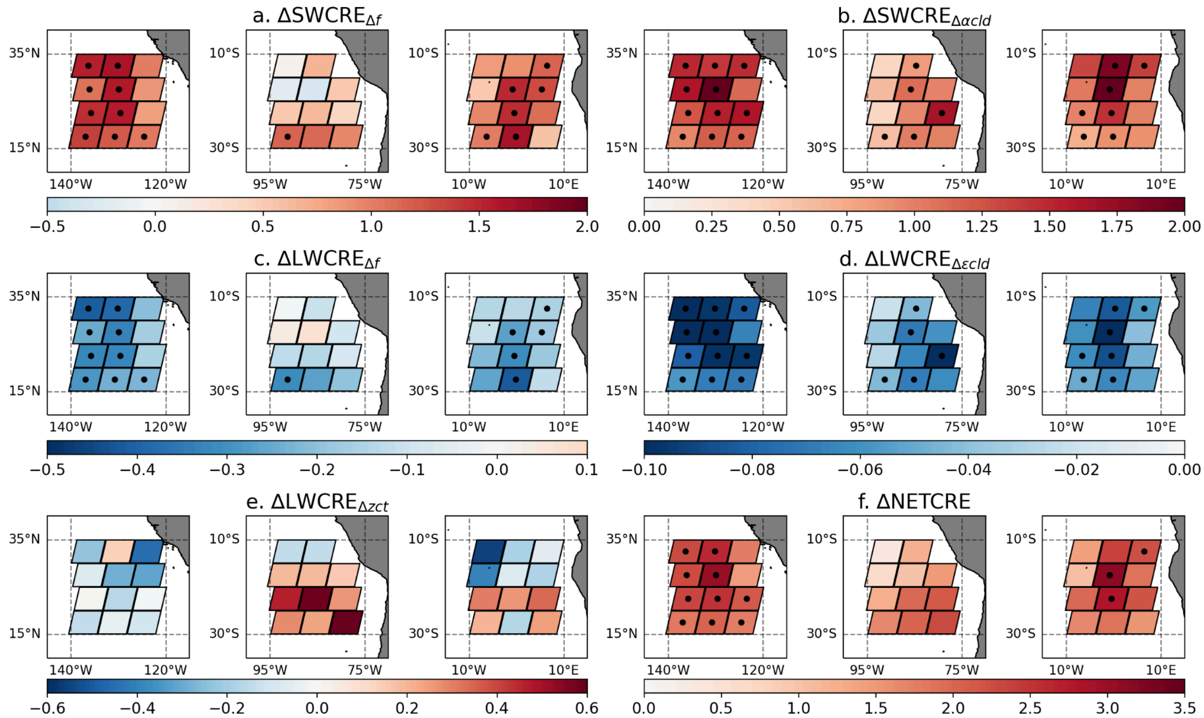

Figure 3.4: Changes in (a) SWCRE due to changes in cloud fraction, (b) SWCRE due to changes in cloud albedo, (c) LWCRE due to changes in cloud fraction, (d) LWCRE due to changes in cloud emissivity, (e) LWCRE due to changes in cloud-top height, and (f) changes in NETCRE from the radiative forcing owing to an instantaneous quadrupling of CO_2. Stippling denotes statistically significant values.

Lastly, we calculate the percentage change from the CRE climatological mean for each grid box, as shown in Figure 3.5. Reductions due to ΔSWCRE range from -0.6 % to -8.3 %, with the most substantial decreases occurring in the NEP where $\Delta SWCRE_{\Delta \alpha cld}$ and $\Delta SWCRE_{\Delta f}$ are both large. Variations in LWCRE due to changes in cloud properties from increased LW↓ are primarily driven by $\Delta LWCRE_{\Delta f}$ and $\Delta LWCRE_{\Delta zct}$. Reductions in LWCRE are most pronounced when $\Delta LWCRE_{\Delta f}$ and $\Delta LWCRE_{\Delta zct}$ are negative. A strengthening in LWCRE is found where $\Delta LWCRE_{\Delta f}$ is small and $\Delta LWCRE_{\Delta zct}$ is positive.

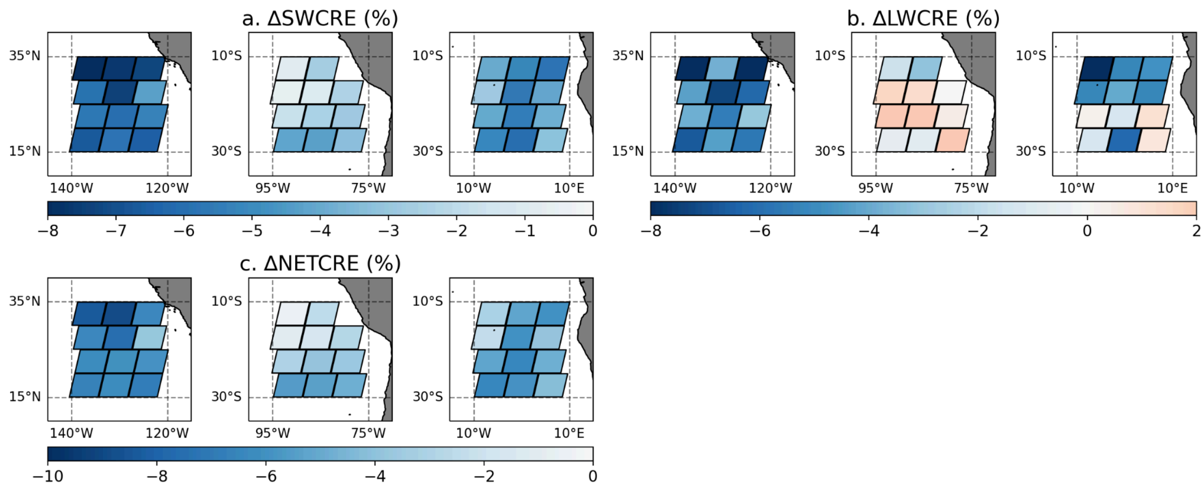

Figure 3.5: Changes in (a) shortwave, (b) longwave, and (c) net cloud radiative effects as shown as the percentage change from the climatological value. Negative values indicate a weakening of the cloud radiative effect while red values indicate a strengthening of the cloud radiative effect due to the radiative forcing from an instantaneous quadrupling of CO_2.

3.4. The strength of LW↓ as a cloud-controlling factor

As described in the previous section, we found that CREs are weakened when LW↓ is increased. This weakening leads to another question: what is the importance of downward longwave radiation relative to other cloud-controlling factors? Cloud property and cloud-controlling factor data are standardized in terms of Z-score, which is the difference between each value and the mean divided by the standard deviation. Standardized data is analyzed using the multiple linear regression method for each 5° latitude x 6.2° longitude grid box. This method is then repeated with LW↓ omitted to provide a benchmark by which we can compare the confounding influence of LW↓ on other CCFs. Figure 8 compares the standardized cloud property and CCF regression coefficients when LW↓ is included and omitted as an independent CCF. This figure displays the typical cloud property anomaly resulting from a typical CCF anomaly when all other CCFs are held constant. The key finding is that cloud fraction and LWP are negatively influenced more by changes in LW↓ than any other CCF.

Estimated inversion strength is also very influential on cloud fraction and LWP but with the opposite sign than LW↓. Low-level temperature advection, RH_{3000m}, WS, and ω_{700hPa} all exhibit similar influence in terms of magnitude on fraction and LWP. Cold temperature advection, higher above-cloud relative humidity, stronger low-level wind speed, and increased subsidence are associated with increased fraction and LWP.

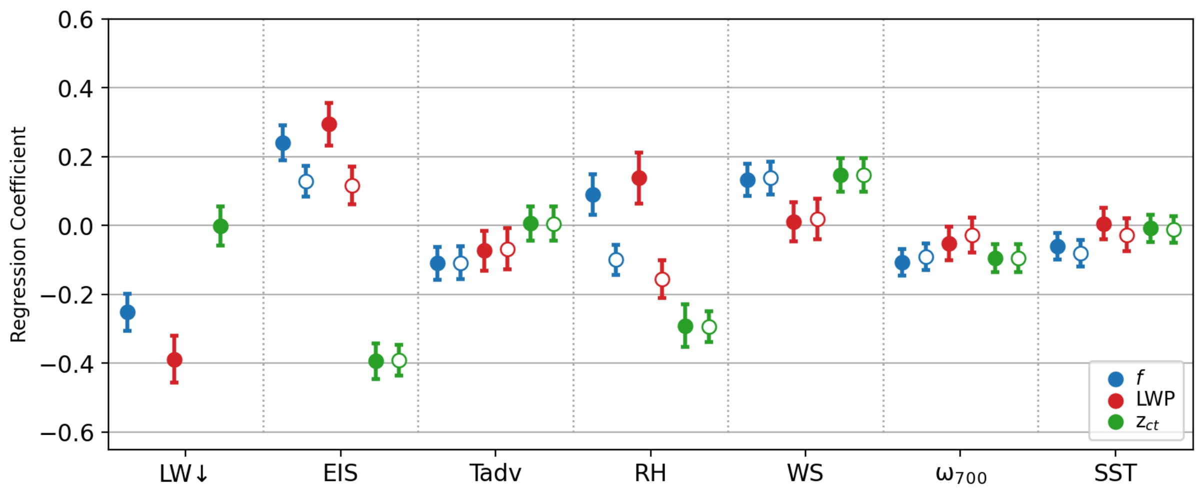

Figure 3.6: Standardized cloud property and CCF regression coefficients when LW↓ is included (in colored circles) and omitted (in white circles). The error bars represent the 95% confidence intervals.

We find no meaningful relationship between cloud-top height and LW↓, which is consistent with our previous findings. Estimated inversion strength is the most influential CCF on cloud-top height, with stronger temperature inversions associated with lower cloud-top heights. A strong temperature inversion reduces entrainment at the cloud top, thereby minimizing drying and deepening of the boundary layer. Relative humidity is the second most influential CCF on cloud-top height, with greater humidity leading to lower cloud-top heights. This is because humid air entrained into the cloud top moistens the cloud layer, resulting in less evaporative cooling, thereby restricting boundary layer deepening and rising cloud tops (Eastman and Wood 2018). A positive relationship between WS and z_{ct} is found, and it is significant at a 95% confidence level. Stronger near-surface level winds increase moisture in the boundary layer, amplifying convection and elevating z_{ct}. Increased subsidence reduces cloud-top height, as an increase in subsidence squeezes the boundary layer, limiting cloud-top height.

Removing LW↓ as a CCF changes the influence of RH_{3000m} and EIS on fraction and liquid water path. The sign of the influence RH_{3000m} has on fraction and LWP is reversed, with moist air favoring less cloud fraction and LWP when LW↓ is not included as a CCF. This is against the traditional understanding of above-cloud RH as a CCF (Van Der Dussen et al. 2015; Myers and Norris 2016; Scott et al. 2020). To understand this change in sign, note that RH_{3000m} and LW↓ are correlated but have opposing influences on fraction and LWP. Even though the entrainment of humid air increases fraction and LWP, the increase in LW↓ associated with humid air has a stronger effect, causing a net decrease in fraction and LWP. We also find that EIS has less influence on fraction and LWP when LW↓ is excluded as a CCF. This may be because stronger temperature inversions are associated with warmer air above the cloud top. Warmer air will emit more downward longwave radiation, which will partly counteract the effects a stronger temperature inversion has on fraction and LWP.

3.5. Summary of Regional Study Results

Two different methods were developed to quantify the relationships between low-level cloud properties and LW↓ over the eastern subtropical oceans. Both methods achieved similar results, revealing a robust relationship between low-level cloud properties and LW↓. Lower cloud fraction and decreased liquid water path were associated with increased LW↓. The relationship between LW↓ and cloud-top height was positive but not significant. While both LWCRE and SWERE were weakened by LW↓, the change in SWCRE was approximately ten times larger than that in LWCRE, thus dominating the change in NETCRE. We found reductions in cloud fraction and albedo weakened SWCRE, whereas reductions in cloud fraction and cloud emissivity weakened LWCRE. Increases in cloud-top height with LW↓ provided an opposing component and were strong enough to occasionally change the sign of the relationship between LW↓ and LWCRE. Altogether, the change in NETCRE was approximately 2 Wm^{-2}, indicating that when LW↓ was increased by an amount equivalent to the radiative forcing from $4xCO_2$, the cloud radiative effect of low-level clouds in the stratocumulus regions was reduced by 5 %. Cloud fraction and liquid water path were observed to be more sensitive to changes in LW↓ than any other CCFs.

We found a negative relationship between LW↓ and the two cloud properties, wherein increased LW↓ reduced *f* and LWP when other CCFs are held constant. These relationships were explained by the radiative mechanism by which low-level clouds generate most of their convection. There is strong LW radiative cooling at the cloud top because of the difference in upward LW emission from the cloud and downward LW emission from the atmosphere above. A more emissive atmosphere, and subsequently more LW↓, reduces this LW difference, thereby reducing LW radiative cooling. Consequently, there is less convective overturning, and cloudiness decreases. Downward longwave radiation displayed confounding effects on RH and EIS. When not accounted for, the cloud-reducing effect of LW↓ weakened the influence of RH and EIS on low-level cloud fraction and LWP.

The small size of the three regions was a restriction of this study. While the three regions contained tens of thousands of observations, they comprised a small part of the global ocean. Our results on the relationship between cloud-top height and LW↓ were inconclusive. A previous study found that increased LW↓ lowered cloud-top height, while we saw the effect as slightly positive but not statistically significant (Christensen et al. 2013). The global study in the remainder of this document will expand the observation areas and provide substantial insight into the effect LW↓ has on low-level cloud-top height, particularly in locations where low-level clouds other than stratocumulus are commonly found. Due to the agreement between the compositing and multilinear regression methods, the latter is found to be a valid approach for the rest of the global ocean.

Acknowledgments

Chapter 3 contains material currently being prepared for submission for publication. Christopher Macpherson; and Norris, Joel. "The Effects of Downward Longwave Radiation on Low-Level Clouds: A Regional Analysis". The dissertation author was the primary investigator and author of this paper.

Chapter 4 Data and Methods of the Global Study

Continuing the initial work described in the previous chapters, we move from studying three small stratocumulus regions to the global ocean. The following chapters use the same CRE derivations, datasets, and methods described in Chapter 2 with a few modifications. For brevity, we describe only the main points of the methodology in this chapter. The primary dataset is the NASA A-Train Integrated CALIPSO, CloudSat, CERES, and MODIS dataset version RelB1. The CCCM dataset provides cloud, radiative, and meteorological data organized onto CERES footprints. We utilize the vertical flux profile to obtain LW↓ at the uppermost extent of the boundary layer and the vertical cloud profile to obtain low-level cloud properties even while upper-level clouds are present in the same vertical column.

Along with CCCM, we use NASA CERES Flux by Cloud Type, SYN1deg, and Modern Era Retrospective-analysis for Research and Application Version 2 datasets to provide parameters not included in CCCM. The FBCT dataset supplies LW radiative flux reaching the top of the atmosphere that originates from low-level clouds, cloud emissivity, cloud albedo, and cloud-top temperature. The SYN1deg dataset provides clear-sky LW and SW radiative fluxes. The MERRA-2 dataset offers meteorological parameters in wind speed and air temperature at 985 hPa and vertical pressure velocity at 700 hPa.

We use data from 60° N to 60° S and from 01/01/2007 to 12/31/2010. Only CCCM footprints with a majority liquid water surface type are included. As described in previous chapters, low-level clouds are clouds with a cloud-top height below 3 km. Because each CCCM footprint can contain up to 16 cloud groups, we average the first cloud-top height below 3 km across the 16 possible cloud groups, weighted by cloud group fraction, to obtain a single low-level cloud-top height for each CCCM footprint. CCCM data is un-gridded and repeats over the same location every 16 days. Data from FBCT, SYN1deg, and MERRA-2 are aligned to CCCM data using the methodology described in Chapter 2. Data is then averaged by 5° latitude, approximately 25 consecutive footprints. Any 5° latitude average that contains fewer than 20 footprints is removed. Only nighttime profiles are used because SW radiation causes heating at the cloud top (Christensen et al. 2013). This effect cannot be easily separated from the effect of LW radiation. Using nighttime-only profiles mitigates this issue. We calculate deseasonalized anomalies for cloud and meteorological parameters from the Fast-Fourier Transform constructed seasonal cycle.

Grid boxes of approximately 6.2° longitude and 5° latitude are organized into different regimes, following the same methodology as Scott et al. (2020), creating stratocumulus, trade cumulus, tropical ascent, and midlatitude regimes for low-level clouds based on climatological EIS and ω_{700hPa}. We make one modification to the regime criteria for grid boxes equatorward of 25° latitude with weak subsidence ($\omega_{700hPa} > 0$ hPa) and a positive temperature inversion (EIS > 1°C). Grid boxes matching these criteria are included with the stratocumulus regime. The locations of the regimes are displayed in Figure 4.1 and are in good agreement with Scott et al. (2020). Grid boxes that contain fewer than 250 5°-latitude track averages are omitted. These grid boxes lack data due to CERES observations over land or sea ice instead of liquid water. Variance inflation factors for CCFs are less than ten at every grid box, with a mean value of approximately four. Low variance inflation factors are indicative of low CCF multicollinearity.

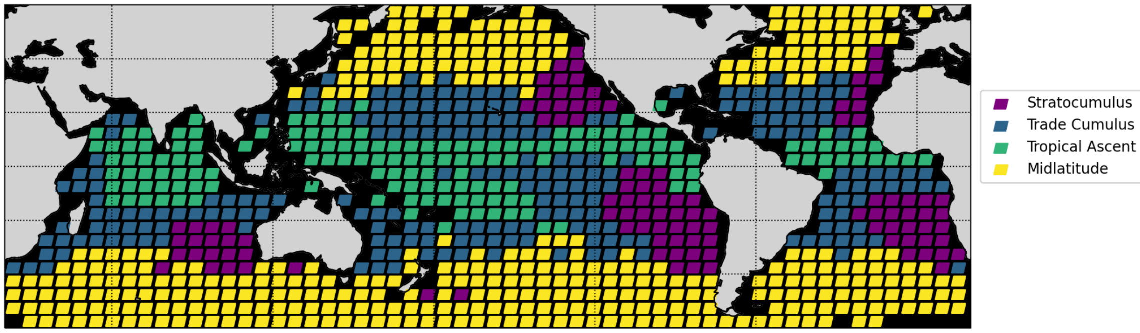

Figure 4.1: Locations of the low-level cloud regimes. Grid boxes with fewer than 250 data points are not displayed.

At each grid box, linear regressions are calculated between daytime observations of LWP from CCCM and cloud albedo and cloud emissivity from FBCT following the method described in Chapter 2.3. We then use the linear regression coefficients obtained at each grid box to convert nighttime retrievals of CCCM LWP to cloud albedo and cloud emissivity. This differs from the regional study because the linear regression coefficients are calculated on a grid box basis instead of single values across all regions.

Acknowledgments

Chapter 4 contains material currently being prepared for submission for publication. Christopher Macpherson; and Norris, Joel. "The Effects of Downward Longwave Radiation on Low-Level Clouds: A Global Analysis". The dissertation author was the primary investigator and author of this paper.

Chapter 5 Results of the Global Study

5.1. Climatology of low-level cloud properties, cloud-controlling factors, and cloud radiative effects

We begin by discussing the climatology of low-level cloud properties. Cloud fraction peaks in the stratocumulus regimes and over the Southern Ocean and is the lowest in the Northern Indian Ocean and the tropical warm pool region (Fig. 5.1a.). Upper-level clouds, or clouds with base heights above 3000 m, are most abundant over the tropical warm pool and along the equator, where the Intertropical Convergence Zone is located (Fig 5.1b). The climatology of cross-boundary clouds, clouds with cloud-top heights above 3000 m but cloud-base heights below 3000 m, is shown in Figure 5.1c. Cross-boundary clouds occur with some frequency poleward of 45° in both hemispheres, along the equator, and over the warm pool, while mostly absent in the stratocumulus regime. Liquid water path in the boundary layer is highest in the stratocumulus regime and lowest in the warm pool and Northern Indian Ocean. Cloud-top heights are lowest along the coast in the eastern subtropics and rise westward, displaying the stratocumulus-to-cumulus transition (Klein and Hartmann 1993; Albrecht et al. 1995). The climatologies of cloud emissivity and cloud albedo are shown in Figures 5.1f and 5.1g. The midlatitude storm tracks and stratocumulus regions are distinguishable by having high cloud emissivity and cloud albedo. In contrast, the trade cumulus and equatorial regions have low cloud emissivity and albedo.

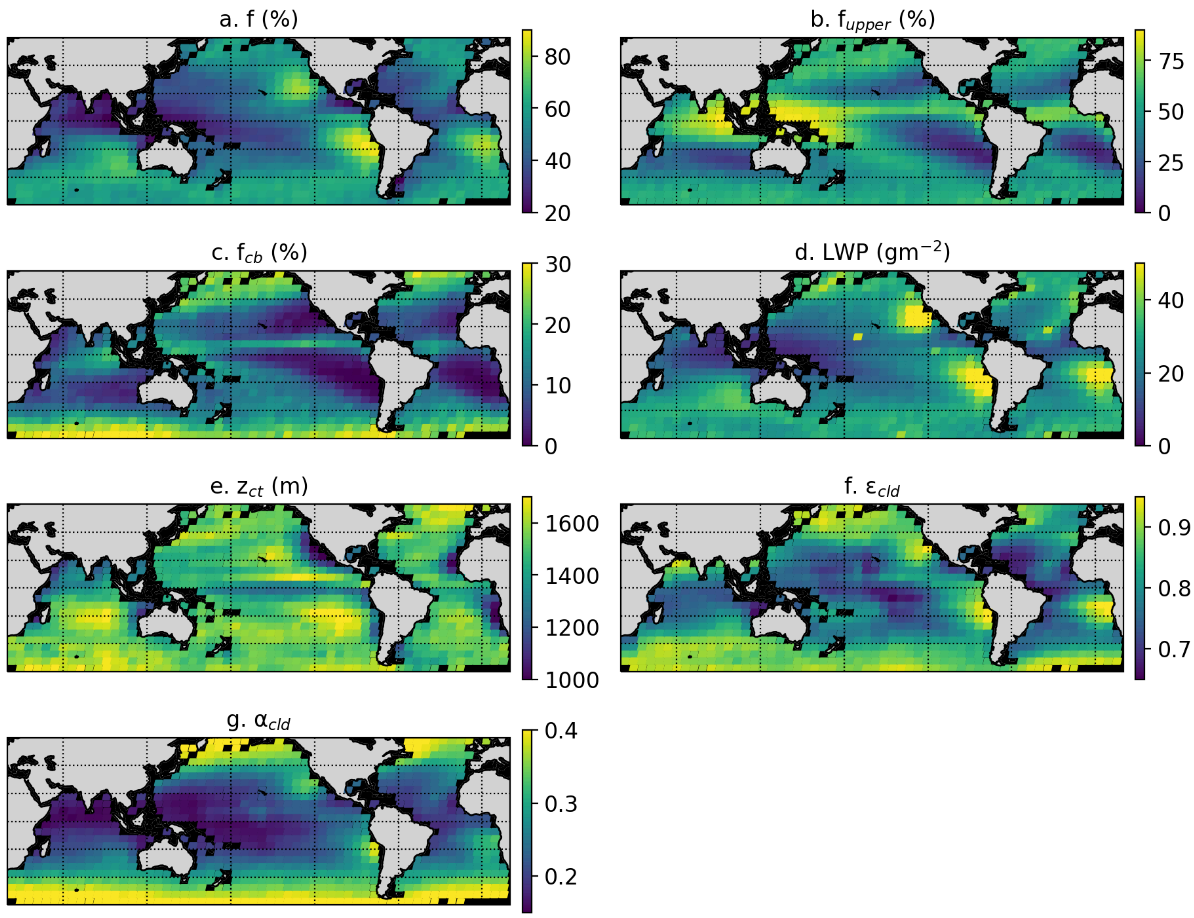

Figure 5.1: Climatological averages for a. low-level cloud fraction, b. upper-level cloud fraction, c. cross-boundary cloud fraction, d. boundary layer liquid water path, e. low-level cloud-top height, f. low-level cloud infrared emissivity, and g. low-level clouds albedo. Grid boxes with fewer than 250 data points are not displayed.

The climatology of seven CCFs is displayed in Figure 5.2. Relative humidity at 3000 m and downward longwave radiation at 3000 m show similar variation given their correlation coefficient (r = 0.65), with both parameters peaking along the equator and the warm pool region (Fig. 5.2a-b). Relative humidity reaches a minimum in the stratocumulus regime, while LW↓ is lowest in the highest latitudes of the study area. Low-level wind speed is between 5 and 10 ms^{-1} for much of the globe except for over the Southern Ocean, where wind speeds are higher (Fig. 5.2c). Estimated inversion strength is depicted in Figure 5.2e, where positive values of EIS are located in the eastern subtropical oceans and the midlatitudes and negative values elsewhere. The climatology of vertical pressure velocity is similar to that of EIS, except for positive values expanding farther into the central tropics and weakly negative values in the midlatitudes (Fig. 5.2g).

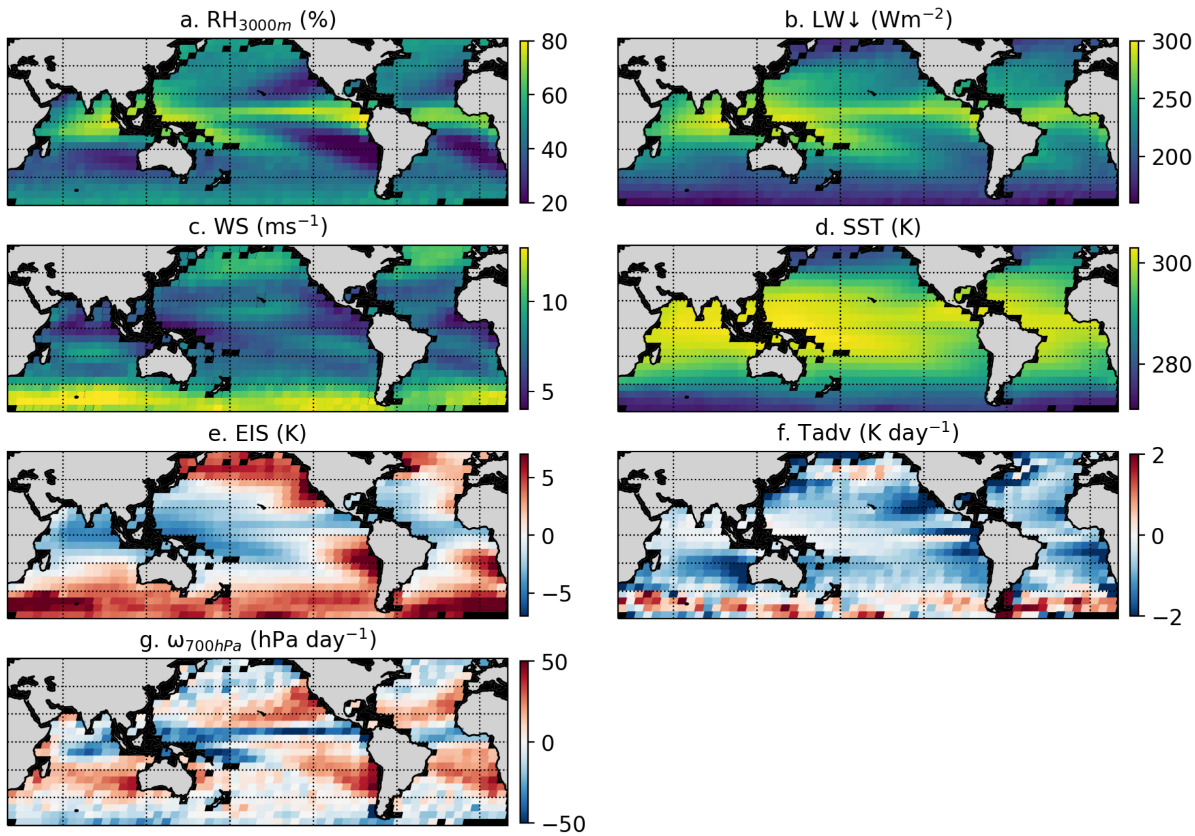

Figure 5.2: Climatological averages for a. relative humidity at 3000 m, b. downward longwave radiation at 3000 m, c. near-surface wind speed, d. sea-surface temperature, e. estimated inversion strength, f. near-surface temperature advection, and g. vertical pressure velocity at 700 hPa. Grid boxes with fewer than 250 data points are not displayed.

For completeness, SWCRE, LWCRE, and NETCRE climatologies are also examined (Fig. 5.3). Climatologies are calculated as the mean cloud radiative effect by low-level clouds that are not obscured by upper-level clouds. Values for SWCRE are negative for all grid boxes and have the largest magnitudes in the stratocumulus regime. Values for LWCRE are positive for all grid boxes and, like SWCRE, have the largest magnitudes in the stratocumulus regime. As the magnitude of SWCRE is approximately four times that of LWCRE, NETCRE is negative at all grid boxes.

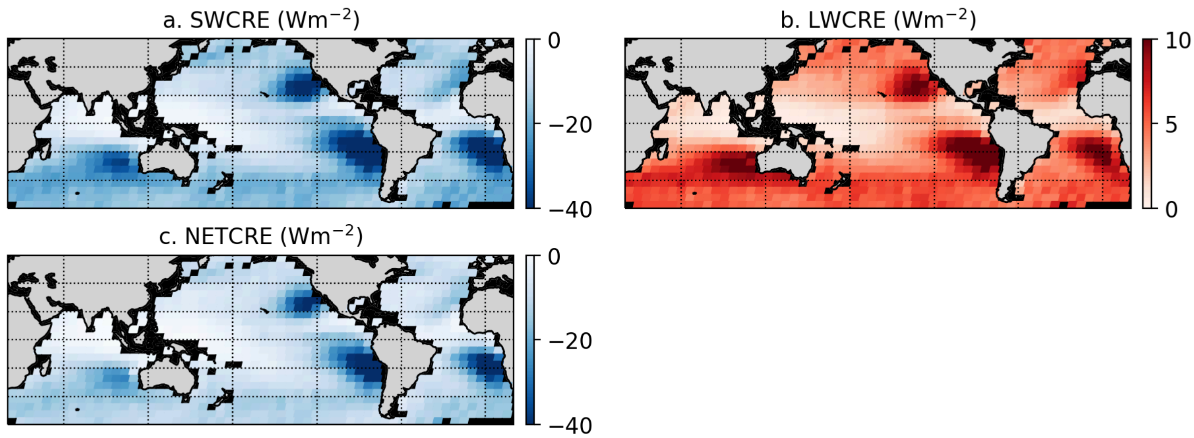

Figure 5.3: Climatological averages for a. shortwave cloud radiative effect, b. longwave cloud radiative effect, and c. net cloud radiative effect. Grid boxes with fewer than 250 data points are not displayed.

5.2. The response of cloud properties to changes in LW↓

To quantify the impact of LW↓ on low-level cloud properties, we use multiple linear regression analysis to isolate the relationships between LW↓ and cloud fraction, boundary layer liquid water path, and cloud-top height. We incorporate six documented (Klein et al. 2017; Scott et al. 2020) cloud-controlling factors along with LW↓ into the analysis: sea-surface temperature, estimated inversion strength, low-level wind speed, low-level temperature advection, relative humidity at 3000 m, and vertical pressure velocity at 700 hPa. These cloud-controlling factors are entered as predictor variables into the multiple linear regression analysis. Additionally, f_{cb} is included as a predictor variable because it directly impacts LW↓ at 3000 m. A cloud spanning the 3000 m boundary will emit more LW↓ than a clear sky will. Each cloud property is entered as a dependent variable in the analysis, and the resulting regression coefficients quantify the relationship with LW↓. The regression coefficients $\partial f/\partial$LW↓, ∂LWP/∂LW↓, and $\partial z_{ct}/\partial$LW↓ reveal the change in cloud property with LW↓ when all other cloud-controlling factors are held constant. Figure 5.4 displays the cloud fraction, liquid water path, and cloud-top height regression coefficients with LW↓ at each grid box. Cloud fraction is found to decrease with increased LW↓. This negative relationship is found in 99% of grid boxes and is significant in approximately three-quarters of grid boxes. There is little variability in $\partial f/\partial$LW↓ except for in the southeastern tropics of the Pacific and Atlantic oceans, where $\partial f/\partial$LW↓ is weakly negative or slightly positive. However, $\partial f/\partial$LW↓ is not statistically significant in these gridboxes. Liquid water path in the boundary decreases globally with increased LW↓. Values for ∂LWP/∂LW↓ are negative for more than 99% of gridboxes, and nearly nine-tenths of regression coefficients are statistically significant. The strongest coefficients are found in the midlatitude regime as well as the eastern areas of the stratocumulus regime. The response of cloud-top height to increased LW↓ is negative but more variable than the other cloud properties. Values for $\partial z_{ct}/\partial$LW↓ are negative in 75% of gridboxes but statistically significant in only 4% of gridboxes. The strongest negative coefficients are found in the tropics, while the strongest positive coefficients are located in the Northern Indian Ocean and subtropics of both hemispheres.

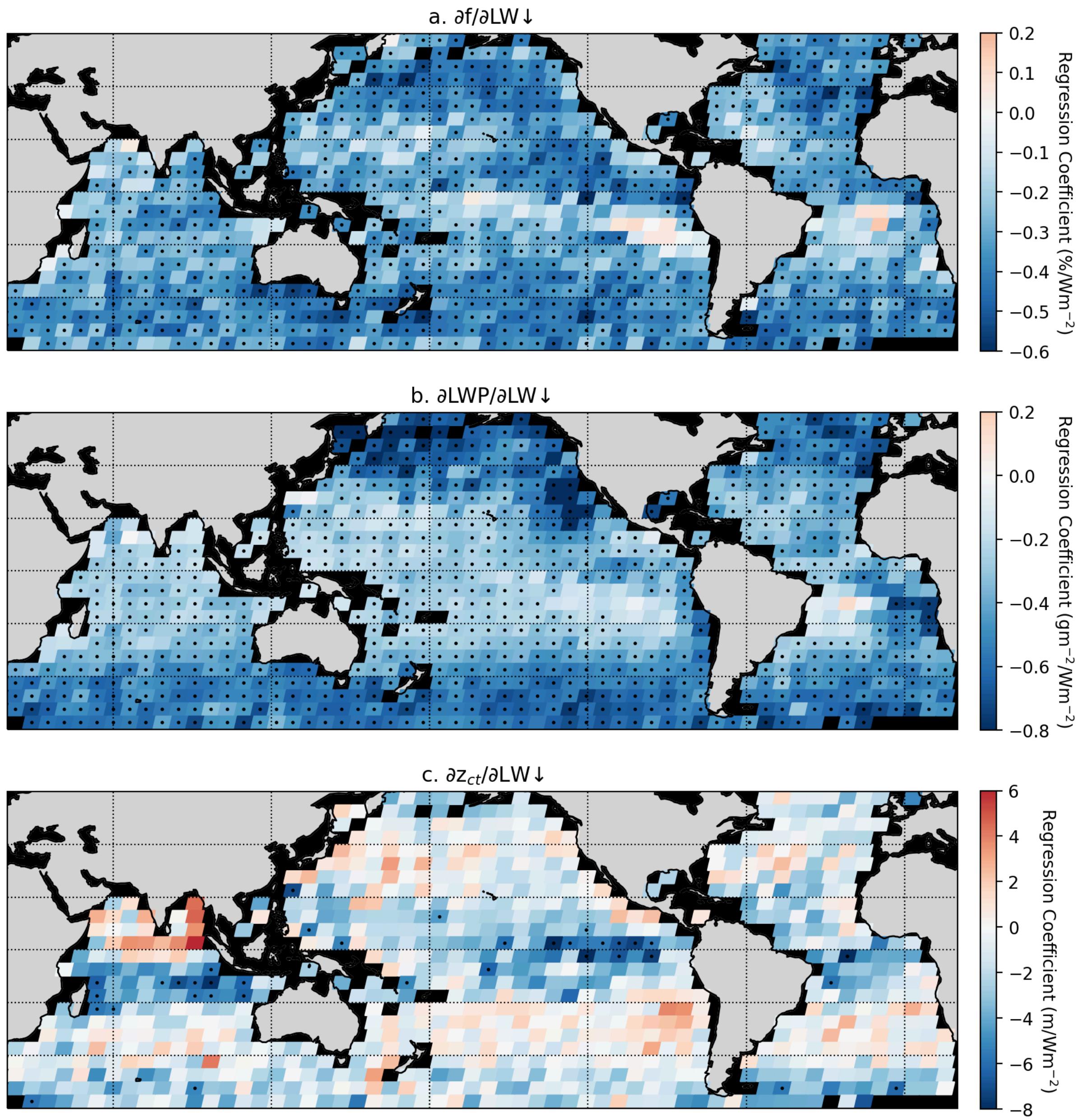

Figure 5.4: Regression coefficients from the multiple linear regression analysis for a. cloud fraction with downward longwave radiation, b. liquid water path with downward longwave radiation, and c. cloud-top height with downward longwave radiation. A negative regression coefficient indicates a decrease in cloud property with increased LW↓. Stippling denotes statistically significant grid boxes. Grid boxes with fewer than 250 data points are not displayed.

Regression coefficients are averaged and weighted by area and number of observations per grid box in each regime and globally. Across all regimes, *∂f*/∂LW↓, ∂LWP/∂LW↓, and ∂z_{ct}/∂LW↓ are negative and significant at a 95% confidence level. Cloud fraction is reduced by LW↓ in similar amounts across regimes, except for the midlatitude regime, where fraction is more strongly reduced. The largest reductions in LWP with LW↓ occur in the midlatitude and stratocumulus regimes, while the largest reductions in z_{ct} with LW↓ occur in the trade cumulus and tropical ascent regimes. Globally, LW↓ reduces cloud fraction by -0.32 ± 0.01 % / Wm^{-2}, liquid water path by -0.40 ± 0.01 gm^{-2} / Wm^{-2}, and cloud-top height by -1.41 ± 0.16 m / Wm^{-2}.

Table 5.1**:** The average low-level cloud property regression coefficient with LW↓ for each regime and the globe. Averages are weighted by the number of observations per grid box and area with 95% confidence intervals.

	Strato-cumulus	Trade Cumulus	Tropical Ascent	Midlatitude	Global
∂f/∂LW↓ (% / Wm^{-2})	-0.28 ± 0.03	-0.26 ± 0.02	-0.31 ± 0.02	-0.38 ± 0.01	-0.32 ± 0.01
∂LWP/∂LW↓ (gm^{-2} / Wm^{-2})	-0.44 ± 0.04	-0.30 ± 0.02	-0.28 ± 0.02	-0.54 ± 0.02	-0.40 ± 0.01
∂z_{ct}/∂LW↓ (m / Wm^{-2})	-0.75 ± 0.45	-1.92 ± 0.33	-1.79 ± 0.39	-1.03 ± 0.24	-1.41 ± 0.16

Regression coefficients are multiplied by 7.2 Wm^{-2} to simulate the increase in radiative forcing under 4xCO_2 conditions (ΔLW↓) (Zhang and Huang 2014). The resulting changes in cloud fraction, liquid water path, and cloud-top height due to ΔLW↓, as expressed in the percentage change from the climatological average, are shown in Table 5.1. The largest reduction in cloud fraction occurs in the tropical ascent regime. While this regime was not the most sensitive to absolute changes in cloud fraction because the amount of low-level cloud fraction is small (Fig. 5.1a.), minor variations in fraction can induce major changes relative to the climatological average. For the same reason, the greatest reductions in LWP occur in the tropical ascent regime. The largest climatological reductions in cloud-top height are found in the trade cumulus regimes, with ΔLW↓ associated with a decrease in cloud-top height of approximately 1%. Globally, ΔLW↓ reduces cloud fraction by -4.68 ± 0.12 %, liquid water path by -11.89 ± 0.30 %, and cloud-top height by -0.69 ± 0.08 %. This result indicates that ΔLW↓reduces LWP more than f, and changes in z_{ct} are minimal.

Table 5.2: The percentage change in climatological cloud fraction, liquid water path, and cloud-top height due to a perturbation in LW↓ from the radiative forcing of an instantaneous increase in 4xCO_2 for each regime and the globe. Averages are weighted by area and the number of observations per grid box with 95% confidence intervals.

	Strato-cumulus	Trade Cumulus	Tropical Ascent	Midlatitude	Global
Fraction (%)	-3.08 ± 0.38	-4.54 ± 0.30	-7.11 ± 0.41	-5.13 ± 0.17	-4.68 ± 0.12
Liquid Water Path (%)	-8.60 ± 0.84	-10.65 ± 0.80	-19.95 ± 1.37	-13.67 ± 0.45	-11.89 ± 0.30
Cloud-top Height (%)	-0.41 ± 0.25	-0.99 ± 0.17	-0.95 ± 0.20	-0.48 ± 0.12	-0.69 ± 0.08

5.3. Changes in cloud radiative effect with ΔLW↓

Following the traditional definition of CRE, a positive change weakens SWCRE, whereas a negative change weakens LWCRE. The regression coefficients from each grid box are entered into the cloud radiative effect equations. We then produce maps of the change in

SWCRE due to variations in cloud fraction ($\Delta SWCRE_{\Delta f}$) and cloud albedo ($\Delta SWCRE_{\Delta \alpha cld}$). Additionally, maps of change in LWCRE due to variations in cloud fraction ($\Delta LWCRE_{\Delta f}$), cloud emissivity ($\Delta LWCRE_{\Delta \varepsilon cld}$), and cloud-top height ($\Delta LWCRE_{\Delta zct}$) are also constructed. We first examine the changes in SWCRE due to variations in cloud fraction caused by ΔLW↓ (Fig. 5.5a.). The response to ΔLW↓ is positive in 99% of grid boxes and is statistically significant in 68% of grid boxes. The midlatitude and stratocumulus regimes display the strongest response, whereas the response in the trade cumulus and tropical ascent regimes is the weakest, mirroring the $\partial f/\partial$LW↓ results. Due to nearly all grid boxes exhibiting a reduction in cloud fraction with LW↓, SWCRE is weakened because there is less cloud-covered area to reflect SW radiation. The change in SWCRE due to variations in low-level cloud albedo is positive for 97% of grid boxes and statistically significant in 60% of them (Fig. 5.5b.). The stratocumulus regime exhibits the largest response to variations in cloud albedo. A positive change in SWCRE, or weakening, occurs because as cloud albedo decreases with LW↓, clouds reflect less SW radiation to space and are more similar in albedo to the ocean below. The magnitude of $\Delta SWCRE_{\Delta \alpha cld}$ is typically smaller than $\Delta SWCRE_{\Delta f}$, except in areas of the stratocumulus regime where the two ΔCRE components are comparable.

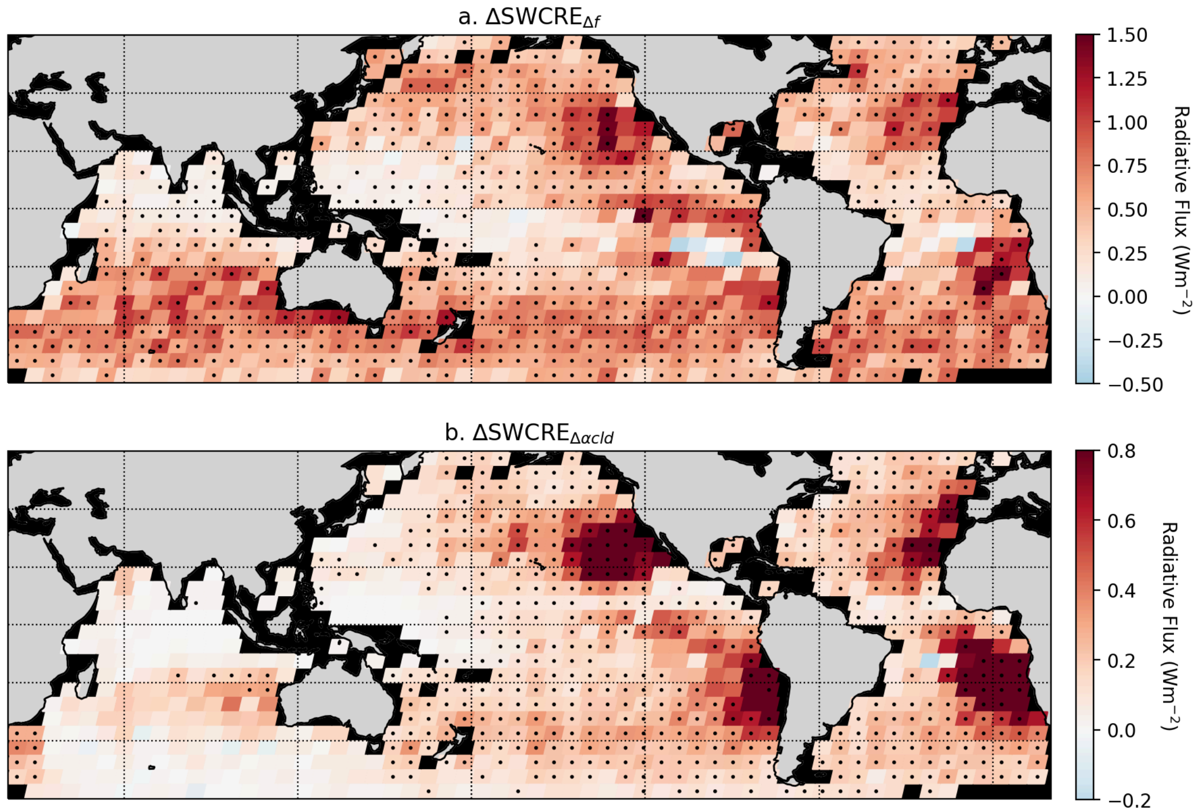

Figure 5.5: Changes in SWCRE resulting from variations in a. cloud fraction with ΔLW↓ and b. cloud albedo with ΔLW↓. Red boxes indicate a weakening of SWCRE, while blue boxes indicate a strengthening of SWCRE. Stippling denotes statistically significant grid boxes. Grid boxes with fewer than 250 data points are not displayed.

Values for $\Delta LWCRE_{\Delta f}$ are negative for 99% of grid boxes, and 68% are significant, meaning at nearly all grid boxes, LWCRE is weakened (Fig. 5.6a.). A weakening of LWCRE occurs because as cloud fraction is reduced with increased LW↓, there is less low-level cloud to absorb LW radiation emitted from the Earth's surface. We find $\Delta LWCRE_{\Delta \varepsilon cld}$ is negative for 97% of grid boxes but at much smaller magnitudes than $\Delta LWCRE_{\Delta f}$ (Fig. 5.6b.). The largest reductions of $\Delta LWCRE_{\Delta \varepsilon cld}$ occur in the stratocumulus regimes, at approximately -0.10 Wm^{-2}. Values for $\Delta LWCRE_{\Delta \varepsilon cld}$ are relatively small because cloud emissivity is still large despite reductions due to ΔLW↓. A cloud with a lower emissivity is less opaque to LW radiation and, therefore, absorbs less LW radiation emitted by the Earth's surface. Values for $\Delta LWCRE_{\Delta zct}$ are negative for 75% of gridboxes and are more varied than $\Delta LWCRE_{\Delta f}$ or $\Delta LWCRE_{\Delta \varepsilon cld}$ (Fig. 5.6a-c.). The largest negative values are found in the equatorial Indian and Atlantic Oceans and the equatorial eastern Pacific Ocean. A decrease in cloud-top height often accompanies an increase in cloud-top temperature. A warmer cloud-top temperature emits more LW radiation to space than a cooler cloud-top, thereby reducing LWCRE as the cloud-top LW emission is more similar to the LW emission of the Earth's surface. Interestingly, positive values for $\Delta LWCRE_{\Delta zct}$ are found in the subtropics and the Northern Pacific Ocean, coinciding with rising cloud-top height with LW↓.

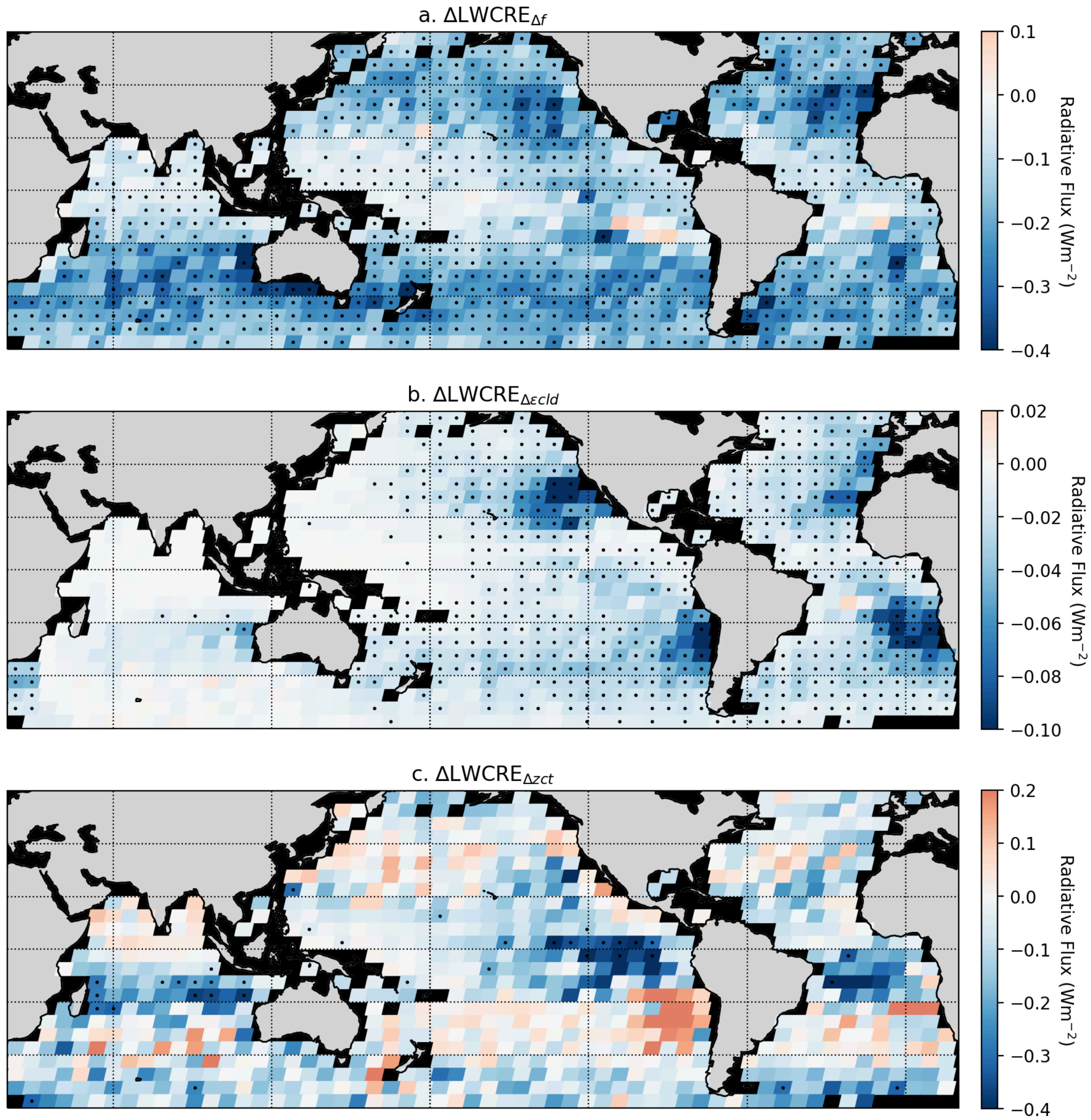

Figure 5.6: Changes in LWCRE resulting from variations in a. cloud fraction with ΔLW↓, b. cloud emissivity with ΔLW↓, and cloud-top height with ΔLW↓. Blue boxes indicate a weakening of LWCRE, while red boxes indicate a strengthening of LWCRE. Stippling denotes statistically significant grid boxes. Grid boxes with fewer than 250 data points are not displayed.

The components of $\Delta SWCRE_{\Delta f}$ and $\Delta SWCRE_{\Delta \alpha cld}$ are summed to make ΔSWCRE or the total change in shortwave cloud radiative effect due to variations in cloud fraction and cloud albedo from ΔLW↓. Of the 877 grid boxes, 99% are positive, and 76% are statistically significant, indicating that the SWCRE is weakened globally (Fig. 5.7a.). The greatest weakening occurs in the stratocumulus regime, particularly over the Pacific and southern Atlantic oceans. The trade cumulus and tropical ascent regimes experience far less change in SWCRE, approximately 0.5 Wm^{-2}, due to a smaller response in $\Delta SWCRE_{\Delta \alpha cld}$. We sum the components of $\Delta LWCRE_{\Delta f}$, $\Delta LWCRE_{\Delta \varepsilon cld}$, and $\Delta LWCRE_{\Delta zct}$ to make ΔLWCRE, or the total change in longwave cloud radiative effect due to variations in cloud fraction, cloud infrared emissivity, and cloud-top height from ΔLW↓. The change in LWCRE due to ΔLW↓ is negative, with 96% of grid boxes exhibiting a decrease in LWCRE, and 32% are statistically significant (Fig. 5.7b.). The largest change is in the North Pacific stratocumulus region, where LW↓ strongly reduces cloud fraction and cloud-top heights. Additionally, notable weakening occurs in the equatorial East Pacific driven by negative $\Delta LWCRE_{\Delta zct}$. Although the weakening of both SWCRE and LWCRE results in offsetting effects, the magnitude of ΔSWCRE is greater than that of ΔLWCRE, and thus ΔNETCRE is positive. Values for ΔNETCRE are positive for 98% of grid boxes, signifying that variations in cloud properties due to ΔLW↓ weaken NETCRE (Fig. 5.7c.). Changes in NETCRE are the largest in the stratocumulus regimes due to significant reductions in cloud albedo and cloud fraction. However, few grid boxes are statistically significant due to the combined uncertainties of the many parameters involved in the ΔNETCRE calculation.

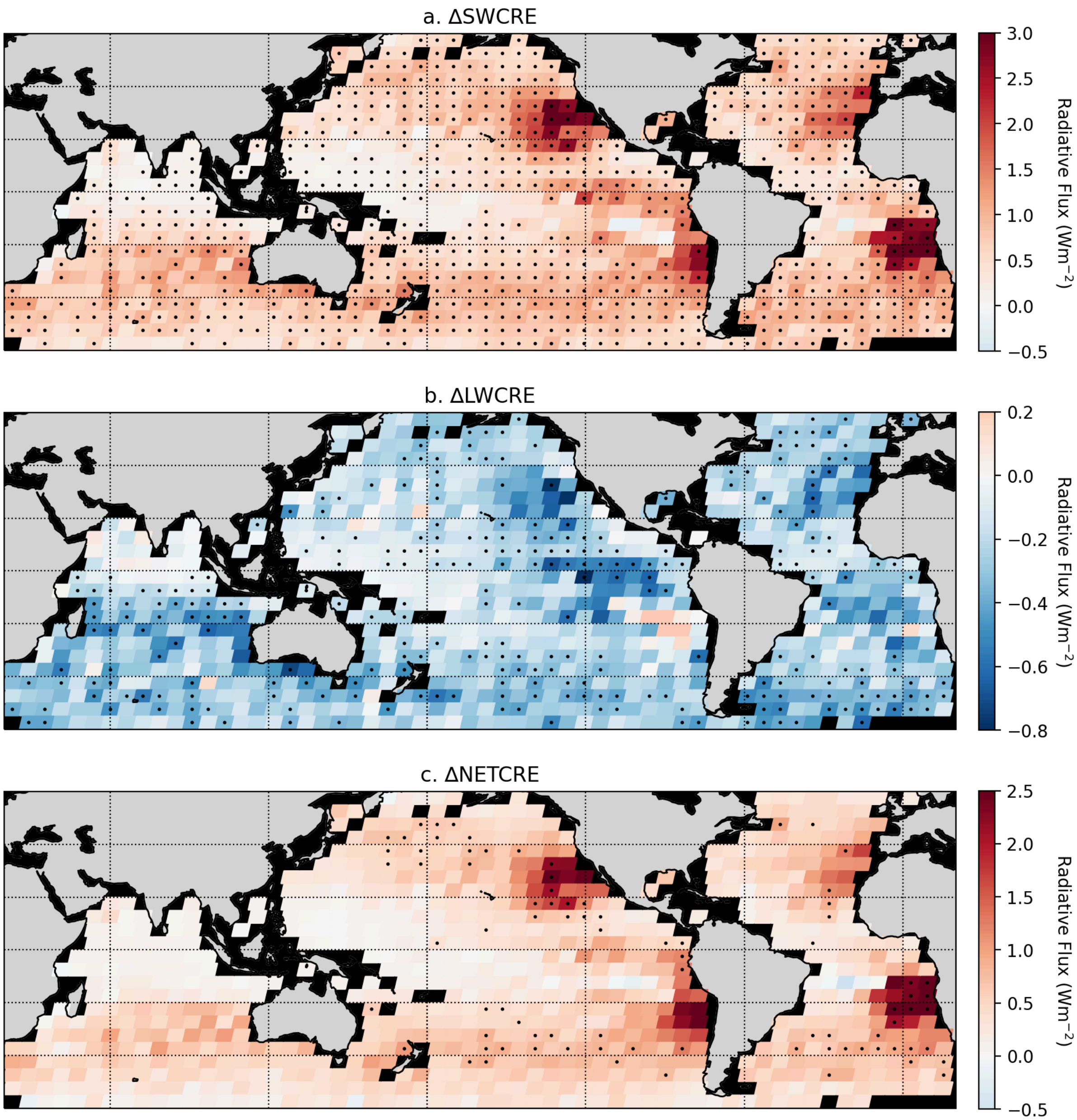

Figure 5.7: Changes in a. SWCRE, b. LWCRE, and c. NETCRE from ΔLW↓. Red boxes indicate a weakening of SWCRE and NETCRE, while blue boxes indicate a weakening of LWCRE. Stippling denotes statistically significant grid boxes. Grid boxes with fewer than 250 data points are not displayed.

Grid box results for changes in CRE components are averaged by regime and globally. These averages, all statistically significant at a 95% confidence level, are presented in Table

5.3. Across all regimes, $\Delta SWCRE_{\Delta f}$ is greater than $\Delta SWCRE_{\Delta \alpha cld}$, indicating that variations in cloud fraction contribute to ΔSWCRE more than variations in cloud albedo. However, in the stratocumulus regime, $\Delta SWCRE_{\Delta f}$ and $\Delta SWCRE_{\Delta \alpha cld}$ are nearly equivalent and are larger than in any other regime. Changes due to reduced cloud fraction with ΔLW↓ are the greatest contributor to ΔLWCRE, with the stratocumulus and midlatitude regimes experiencing the largest reductions in $\Delta LWCRE_{\Delta f}$. Reductions in cloud emissivity have a minimal effect on LWCRE, while decreases in cloud-top height weaken LWCRE. The biggest change in $\Delta LWCRE_{\Delta zct}$ occurs in the trade cumulus regime and is nearly equal to $\Delta LWCRE_{\Delta f}$ in that regime. Globally, ΔSWCRE is three times larger than ΔLWCRE, weakening NETCRE by more than 0.5 Wm^{-2}. The results in ΔCRE are also expressed as the percentage change from the climatological average CRE in Table 5.4. Globally, ΔLW↓ reduces SWCRE by -5.51 ± 0.15 %, LWCRE -6.50 ± 0.29 %, and NETCRE -5.28 ± 0.37 %.

Table 5.3: Changes in cloud radiative effects due to perturbations in LW↓ from the radiative forcing of an instantaneous increase in 4xCO_2 for each regime and the globe. Positive values indicate a weakening of SWCRE and NETCRE, whereas negative values indicate a weakening of LWCRE. Units are in Wm^{-2}. Averages are weighted by area and the number of observations per grid box with 95% confidence intervals.

	Strato-cumulus	Trade Cumulus	Tropical Ascent	Midlatitude	Global
$\Delta SWCRE_{\Delta f}$	0.78 ± 0.10	0.43 ± 0.03	0.26 ± 0.02	0.62 ± 0.02	0.51 ± 0.02
$\Delta SWCRE_{\Delta \alpha cld}$	0.75 ± 0.07	0.20 ± 0.02	0.08 ± 0.01	0.17 ± 0.01	0.24 ± 0.01
$\Delta LWCRE_{\Delta f}$	-0.19 ± 0.02	-0.13 ± 0.01	-0.07 ± 0.01	-0.20 ± 0.01	-0.25 ± 0.01
$\Delta LWCRE_{\Delta \varepsilon cld}$	-0.050 ± 0.005	-0.015 ± 0.001	-0.005 ± 0.001	-0.016 ± 0.001	-0.018 ± 0.001
$\Delta LWCRE_{\Delta zct}$	-0.07 ± 0.05	-0.10 ± 0.02	-0.06 ± 0.01	-0.05 ± 0.01	-0.07 ± 0.01
ΔSWCRE	1.53 ± 0.15	0.63 ± 0.04	0.34 ± 0.02	0.79 ± 0.03	0.75 ± 0.03
ΔLWCRE	-0.31 ± 0.06	-0.24 ± 0.02	-0.14 ± 0.01	-0.27 ± 0.02	-0.24 ± 0.01
ΔNETCRE	1.22 ± 0.19	0.39 ± 0.06	0.20 ± 0.03	0.52 ± 0.04	0.51 ± 0.03

Table 5.4: Changes in climatological cloud radiative effects due to perturbations in LW↓ from the radiative forcing of an instantaneous increase in 4xCO_2 for each regime and the globe. Positive values indicate a weakening of SWCRE and NETCRE, whereas negative values indicate a weakening of LWCRE. Averages are weighted by area and the number of observations per grid box with 95% confidence intervals.

	Strato-cumulus	Trade Cumulus	Tropical Ascent	Midlatitude	Global
SWCRE (%)	-4.60 ± 0.41	-5.42 ± 0.34	-7.03 ± 0.43	-5.06 ± 0.17	-5.51 ± 0.15
LWCRE (%)	-4.32 ± 0.79	-7.17 ± 0.67	-9.12 ± 0.88	-5.27 ± 0.32	-6.50 ± 0.29
NETCRE (%)	-4.74 ± 0.75	-4.84 ± 0.75	-6.73 ± 1.39	-4.99 ± 0.38	-5.28 ± 0.37

5.4. Downward longwave radiation as a cloud-controlling factor

The influence of LW↓ as a cloud-controlling factor is compared to six established CCFs: EIS, Tadv, RH_{3000m}, WS, SST, and ω_{700hPa}. Cloud property and CCF data are standardized by calculating the Z-score and entering it into the multiple linear regression analysis for each grid box. By standardizing the data before conducting the multiple linear regression analysis, data can be compared even though it initially had different units. The regression coefficients in Tables 5.5, 5.6, and 5.7 are interpreted as the anomalous change in cloud property for a standard anomaly change in a CCF. For example, cloud fraction in the stratocumulus regime changes -0.28 ± 0.03 standard deviations for a typical positive anomaly in LW↓. Standardized regression coefficients between cloud fraction and CCFs are displayed in Table 5.5. The largest change in fraction is associated with an anomalous change in LW↓ for 75 % of regimes and is statistically significant in all regimes. This change indicates that LW↓ is the most influential CCF on fraction, with a global average of -0.41 ± 0.01. Downward longwave radiation influences fraction in the midlatitude regime more than in any other regime. However, EIS is slightly more influential than LW↓ on fraction in the stratocumulus regime. The standardized regression coefficients between LWP and the CCFs are displayed in Table 5.6. The largest change in LWP is associated with an anomalous change in LW↓ for all regimes and is statistically significant, showing that LW↓ is the most influential CCF on LWP. The global average for standardized ∂LWP/∂LW↓ is -0.68 ± 0.02. Downward longwave radiation is more influential in the midlatitude regime more than in any other regime. The results for standardized regression coefficients between z_{ct} and LW↓ are shown in Table 5.7. Unlike the previous two cloud properties, LW↓ is not the most influential CCF on cloud-top height. We find LW↓ to be the fourth most influential CCF on z_{ct}, following EIS, WS, and ω_{700hPa}. Nonetheless, the relationship between LW↓ and z_{ct} is significant for all regimes and the global average. Downward longwave radiation influences z_{ct} in the tropical ascent regime more than in any other regime.

Table 5.5: Standardized regression coefficients for cloud fraction and cloud-controlling factors. Averages are weighted by area and the number of observations per grid box with 95% confidence intervals.

	Stratocumulus	Trade Cumulus	Tropical Ascent	Midlatitude	Global
LW↓	-0.28 ± 0.02	-0.34 ± 0.03	-0.44 ± 0.03	-0.49 ± 0.02	-0.41 ± 0.01
EIS	0.30 ± 0.03	0.30 ± 0.02	0.27 ± 0.03	0.38 ± 0.01	0.33 ± 0.01
Tadv	-0.11 ± 0.02	-0.16 ± 0.02	-0.09 ± 0.02	-0.17 ± 0.01	-0.14 ± 0.01
RH_{3000m}	0.12 ± 0.03	0.27 ± 0.03	0.40 ± 0.03	0.17 ± 0.01	0.23 ± 0.01
WS	0.13 ± 0.02	0.21 ± 0.02	0.19 ± 0.02	0.06 ± 0.01	0.13 ± 0.01
SST	-0.03 ± 0.02	0.01 ± 0.02	0.09 ± 0.02	0.0 ± 0.01	0.01 ± 0.01
ω_{700hPa}	-0.11 ± 0.02	-0.08 ± 0.02	-0.04 ± 0.02	-0.08 ± 0.01	-0.08 ± 0.01

Table 5.6: The same as Table 5.5 but for liquid water path.

	Stratocumulus	Trade Cumulus	Tropical Ascent	Midlatitude	Global
LW↓	-0.44 ± 0.04	-0.55 ± 0.03	-0.64 ± 0.04	-0.85 ± 0.03	-0.68 ± 0.02
EIS	0.39 ± 0.04	0.31 ± 0.03	0.19 ± 0.03	0.59 ± 0.02	0.42 ± 0.01
Tadv	-0.09 ± 0.03	-0.16 ± 0.02	-0.07 ± 0.02	-0.22 ± 0.02	-0.16 ± 0.01
RH_{3000m}	0.19 ± 0.04	0.27 ± 0.03	0.25 ± 0.03	0.20 ± 0.02	0.22 ± 0.01
WS	0.04 ± 0.03	0.03 ± 0.02	0.02 ± 0.02	0.02 ± 0.01	0.03 ± 0.01
SST	0.01 ± 0.03	0.03 ± 0.02	0.05 ± 0.03	0.06 ± 0.01	0.04 ± 0.01
ω_{700hPa}	-0.06 ± 0.03	-0.05 ± 0.02	-0.01 ± 0.02	-0.05 ± 0.02	-0.04 ± 0.01

Table 5.7: The same as Table 5.5 but for liquid water path.

	Stratocumulus	Trade Cumulus	Tropical Ascent	Midlatitude	Global
LW↓	-0.05 ± 0.04	-0.12 ± 0.03	-0.14 ± 0.03	-0.10 ± 0.03	-0.10 ± 0.02
EIS	-0.33 ± 0.03	-0.04 ± 0.02	0.08 ± 0.03	-0.34 ± 0.02	-0.19 ± 0.01
Tadv	0.0 ± 0.03	-0.09 ± 0.02	-0.04 ± 0.02	-0.01 ± 0.01	-0.03 ± 0.01
RH_{3000m}	-0.22 ± 0.04	-0.11 ± 0.03	0.12 ± 0.03	0.05 ± 0.02	-0.01 ± 0.01
WS	0.15 ± 0.03	0.14 ± 0.02	0.08 ± 0.02	0.16 ± 0.01	0.14 ± 0.01
SST	-0.03 ± 0.02	-0.02 ± 0.02	0.02 ± 0.02	-0.03 ± 0.01	-0.02 ± 0.01
ω_{700hPa}	-0.10 ± 0.02	-0.11 ± 0.02	-0.07 ± 0.02	-0.11 ± 0.02	-0.10 ± 0.01

We repeat the standardized multiple linear regression analysis with LW↓ excluded as a cloud-controlling factor. Removing LW↓ as an independent variable allows us to search for any confounding effects LW↓ may have on the other CCFs. If LW↓ does not exhibit any confounding effects on a CCF, then its regression coefficient will not change. The comparison of standardized regression coefficients for multiple linear regression analyses with LW↓ included and removed are shown in Figures 5.8, 5.9, and 5.10 for cloud fraction, liquid water path, and cloud-top height. When LW↓ is not included as a CCF in the analysis, $\partial f/\partial$EIS and ∂LWP/∂EIS are smaller in every regime. A less influential EIS can be explained by stronger temperature inversions coinciding with warmer air in the free troposphere above low-level clouds. More downward longwave radiation is emitted by warmer air than by cooler air, which partially weakens the effects stronger EIS has on fraction and LWP. Regression coefficients $\partial f/\partial RH_{3000m}$ and $\partial LWP/\partial RH_{3000m}$ also weaken when LW↓ is not included as a predictor variable. The changes in $\partial LWP/RH_{3000m}$ are so substantial that the direction of the sign changes so that a negative relationship is depicted, even though this is against traditional findings (Van Der Dussen et al. 2015; Eastman and Wood 2018; Scott et al. 2020). This change in sign is explained by the strong correlation between RH_{3000m} and LW↓ and their opposing effects on fraction and LWP. A more humid free troposphere increases fraction and LWP by reducing dry air entrainment and lowering evaporation. However, a more humid free troposphere is also associated with more LW↓, which reduces fraction and LWP by reducing LW cooling the cloud-top.

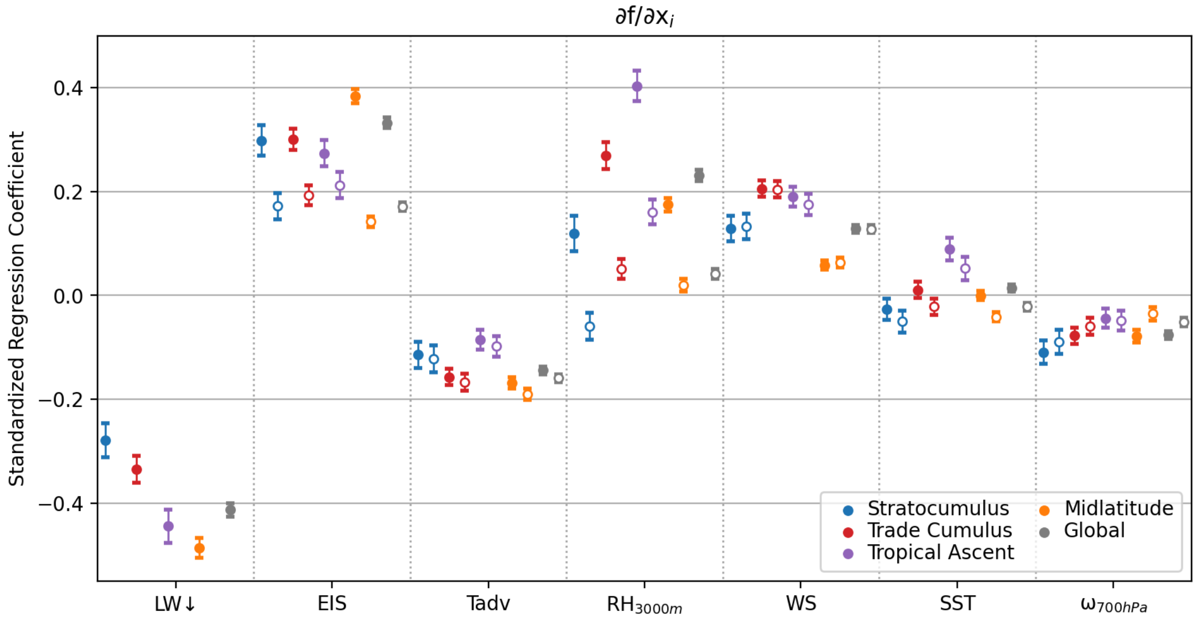

Figure 5.8: Standardized regression coefficients for cloud fraction with CCFs when LW↓ is included as a CCF (in colored circles) and when LW↓ is not included (in white circles) for each regime and the globe. The error bars represent the 95% confidence intervals.

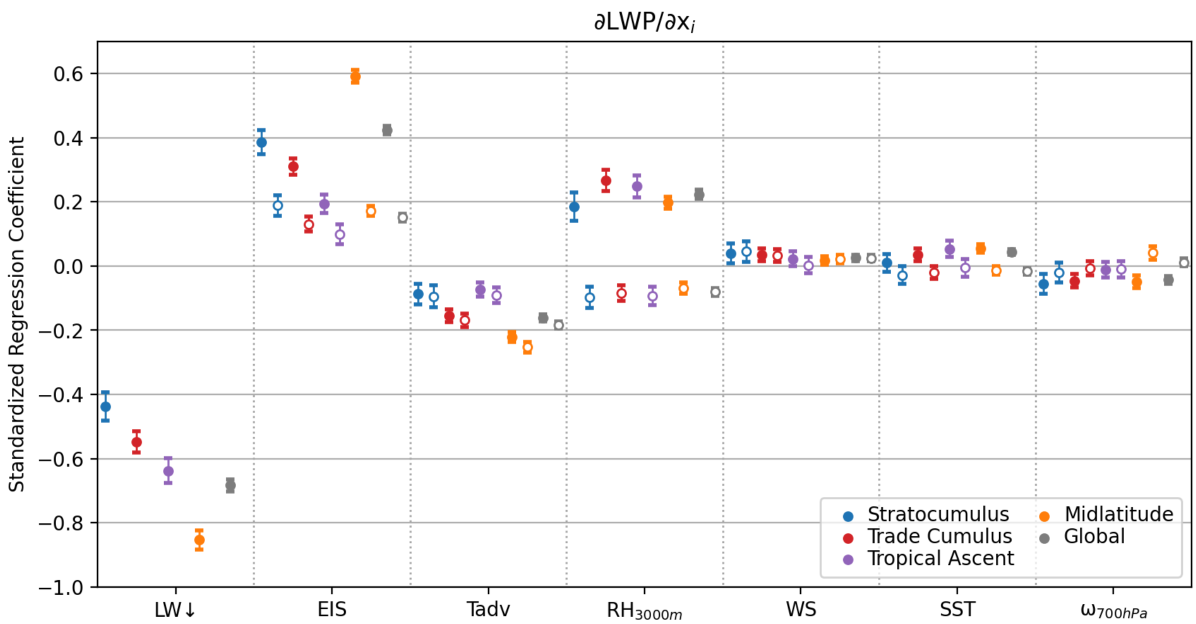

Figure 5.9: The same as Figure 5.8 but for liquid water path.

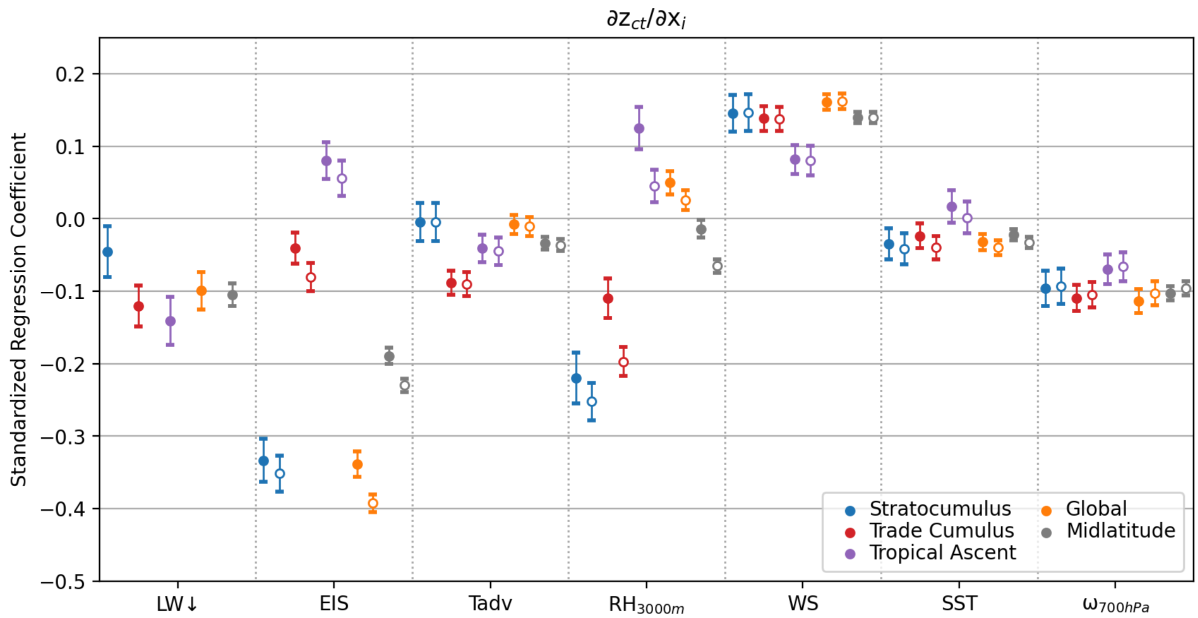

Figure 5.10: The same as Figure 5.8 but for liquid water path.

5.5. Summary of Global Study Results

This study used observations over the global ocean from 60° N to 60°S to measure the effect of downward longwave radiation on low-level cloud fraction, liquid water path, and cloud-top height. We categorized 6.2° longitude and 5° latitude grid box data into different low-level cloud regimes based on climatological EIS and ω_{700hpa}, the results of which agreed with a similar study (Scott et al. 2020). Multiple linear regression allowed us to hold six common cloud-controlling factors constant to obtain regression coefficients between LW↓ and cloud properties. Across all regimes, LW↓ lowered cloud fraction, liquid water path, and cloud-top heights, indicating that LW↓ acted to reduce cloud properties on clouds outside the subtropical eastern oceans.

We also investigated the impact reductions on cloud properties had on the cloud radiative effect. Both the shortwave cloud radiative effect and the longwave radiative effect were weakened when LW↓ was increased to a level equivalent to the radiative forcing from 4xCO_2. As the weakening in the shortwave cloud radiative effect was approximately three times greater than that of the longwave cloud radiative effect, the overall impact was a weakening in the net cloud radiative effect. Lastly, we examined the influence of LW↓ on cloud properties compared to other cloud-controlling factors. We found downward longwave radiation to be the most influential cloud-controlling factor on fraction and LWP. Additionally, LW↓ had confounding effects with EIS and RH_{3000m} for fraction and LWP across all cloud regimes. When LW↓ was not factored as a CCF, the influence of EIS and RH_{3000m} on fraction and LWP was weakened.

Acknowledgments

Chapter 5 contains material currently being prepared for submission for publication. Christopher Macpherson; and Norris, Joel. "The Effects of Downward Longwave Radiation on Low-Level Clouds: A Global Analysis". The dissertation author was the primary investigator and author of this paper.

Chapter 6 Executive Conclusion

Low-level clouds contribute to Earth's energy budget by reflecting shortwave radiation and absorbing and emitting longwave radiation. They vary quickly in time and space and are sensitive to many meteorological conditions. This dissertation aimed to use observations to quantify the impact of downward longwave radiation on low-level cloud properties. By doing this, we would provide an observational analog to simulations investigating the effects of an instantaneous increase in CO_2 on low-level clouds.

The dataset required to achieve this goal required low-level cloud fraction, liquid water path, and cloud-top height. These parameters needed to be available even when upper-level clouds existed in the same area, a typically tricky requirement. A measurement of downward longwave radiation at the top of the boundary layer was needed. The contribution of LW and SW radiation at the top of the atmosphere from low-level clouds and clear skies was likewise needed. Lastly, several meteorological variables were required. As no known dataset contained all of these parameters, we spent significant resources developing a novel dataset that combined parameters from the CCCM, FBCT, SYN1deg, and MERRA-2 datasets on a global scale.

The first study of this dissertation involved low-level clouds over the subtropical eastern oceans. Stratocumulus clouds were frequent over these regions, providing a large occurrence of low-level clouds in three small areas. The regional study used both a compositing and a multiple linear regression analysis to quantify the effect of LW↓ on low-level cloud properties while holding other influential meteorological parameters constant. Changes in free-tropospheric humidity and upper-level clouds caused variations in LW↓.

Downward longwave radiation reduced cloud fraction and LWP while increasing cloud-top height. Due to these relationships, under the radiative forcing due to 4xCO_2, SWCRE and LWCRE were weakened. However, the weakening was not equivalent, resulting in a 5 % reduction in NETCRE for low-level clouds over the subtropical eastern oceans. Both methods achieved similar results, thus validating the use of multiple linear regression analysis in the global study.

The second study of this dissertation was built upon the methodology and findings of the first study. The area of investigation was expanded to the global ocean, organized into differing regimes based on local climatology. Multiple linear regression analysis was performed to once again quantify the effect of LW↓ on low-level cloud properties. Downward longwave radiation, on average, reduced cloud fraction, boundary layer liquid water path, and lowered cloud-top heights across all cloud regimes. Liquid water path was reduced most strongly from the climatological average under the radiative forcing from 4xCO_2, decreasing by approximately 12 %. Cloud fraction was reduced by approximately 5 %, and cloud-top height by 0.7 %. However, variations in cloud fraction, and not LWP, explained most of the change in both SWCRE and LWCRE. At a global average, the change in NETCRE from variations in low-level cloud properties due to a perturbation in LW↓ was negative, weakening NETCRE by 5 %.

The results from both studies provided observational evidence that aligned with modeling and observational studies that have shown that increased LW↓ can reduce cloud fraction, reduce liquid water path, and lower cloud-top heights (Christensen et al. 2013; Kamae and Watanabe 2013; Blossey et al. 2016; Jian et al. 2022). Increased LW↓ acts to warm the cloud-top, partially offsetting cloud-top radiative cooling and weakening the overturning circulation. A weakened circulation reduces entrainment drying, lowering cloud-top heights. It also reduced upward moisture flux from the ocean, decoupling the clouds from the surface and decreasing LWP and fraction. The reduction in cloud properties with increased LW↓ existed across all cloud regimes, indicating that the warming at the cloud top affected clouds regardless of location and climatological conditions. This finding implied that LW↓ reduces cloud properties in both stratocumulus and cumulus clouds. Cloud fraction was decreased by LW↓ at similar rates for all cloud regimes, indicating that LW↓ effects on fraction are consistent. Liquid water path was significantly reduced by LW↓ in the stratocumulus and midlatitude regimes, where climatological fraction and LWP were high. Cloud-top height reductions with LW↓ were more varied than the reductions of fraction and LWP. The global study clarified this relationship, reversing the positive, but not statistically significant, relationship first identified in the regional study. With a much larger sample size, cloud-top height was lowered with LW↓ in all regimes. The variable relationship may have been due to the nature of the CCCM data, where the average cloud-top height was calculated across up to sixteen cloud groups. If LW↓ affected the cloud groups non-uniformly, the cloud-top height response may have been masked. Regardless, the change in cloud-top height with LW↓ was small.

The influence LW↓ had as a cloud-controlling factor was also examined. Cloud fraction and liquid water path were influenced more by changes in LW↓ than by other CCFs. This result was not found for cloud-top height, as several CCFs were more influential than LW↓. Downward longwave radiation has not often been considered a cloud-controlling factor in past studies, or if it has, it has been included with free-tropospheric relative humidity (Blossey et al. 2013; De Roode et al. 2014; Scott et al. 2020; Cesana and Del Genio 2021). The results of this dissertation suggested that LW↓ be considered an important cloud-controlling factor and included with established CCFs. Additionally, LW↓ had confounding effects on EIS and RH_{3000m}. Stronger temperature inversions and higher humidity, while on their own increased cloudiness, were found to have less influence on cloud properties when LW↓ was not included as a CCF. This lowered influence was because stronger temperature inversions and higher humidity were often associated with increased LW↓, which reduced cloudiness. Ultimately, the influence of EIS and RH_{3000m} on low-level clouds may have been underestimated in studies that do not use LW↓ as a CCF. The dataset and methodology developed in this dissertation, along with the subsequent results, provided new insights into the observational effects that downward longwave radiation has on low-level cloud properties and other cloud-controlling factors.

Acknowledgments

Chapter 6 contains material currently being prepared for submission for publication. Christopher Macpherson; and Norris, Joel. “The Effects of Downward Longwave Radiation on Low-Level Clouds: A Global Analysis”. The dissertation author was the primary investigator and author of this paper.

Chapter 7 Bibliography

Albrecht, B. A., C. S. Bretherton, D. Johnson, W. H. Scubert, and A. S. Frisch, 1995: The Atlantic Stratocumulus Transition Experiment—ASTEX. *Bull. Am. Meteorol. Soc.*, **76**, 889–904, https://doi.org/10.1175/1520-0477(1995)076<0889:TASTE>2.0.CO;2.

Arking, A., 1991: The Radiative Effects of Clouds and their Impact on Climate. *Bull. Am. Meteorol. Soc.*, **72**, 795–813, https://doi.org/10.1175/1520-0477(1991)072<0795:TREOCA>2.0.CO;2.

Blossey, P. N., and Coauthors, 2013: Marine low cloud sensitivity to an idealized climate change: The CGILS LES intercomparison. *J. Adv. Model. Earth Syst.*, **5**, 234–258, https://doi.org/10.1002/jame.20025.

——, C. S. Bretherton, A. Cheng, S. Endo, T. Heus, A. P. Lock, and J. J. Van Der Dussen, 2016: CGILS P hase 2 LES intercomparison of response of subtropical marine low cloud regimes to CO_2 quadrupling and a CMIP 3 composite forcing change. *J. Adv. Model. Earth Syst.*, **8**, 1714–1726, https://doi.org/10.1002/2016MS000765.

Bretherton, C. S., 2015: Insights into low-latitude cloud feedbacks from high-resolution models. *Philos. Trans. R. Soc. Math. Phys. Eng. Sci.*, **373**, 20140415, https://doi.org/10.1098/rsta.2014.0415.

——, and P. N. Blossey, 2014: Low cloud reduction in a greenhouse-warmed climate: Results from Lagrangian LES of a subtropical marine cloudiness transition: LAGRANGIAN BOUNDARY-LAYER CLOUD FEEDBACK. *J. Adv. Model. Earth Syst.*, **6**, 91–114, https://doi.org/10.1002/2013MS000250.

——, M. Widmann, V. P. Dymnikov, J. M. Wallace, and I. Bladé, 1999: The Effective Number of Spatial Degrees of Freedom of a Time-Varying Field. *J. Clim.*, **12**, 1990–2009, https://doi.org/10.1175/1520-0442(1999)012<1990:TENOSD>2.0.CO;2.

——, P. N. Blossey, and C. R. Jones, 2013: Mechanisms of marine low cloud sensitivity to idealized climate perturbations: A single‐LES exploration extending the CGILS cases. *J. Adv. Model. Earth Syst.*, **5**, 316–337, https://doi.org/10.1002/jame.20019.

Brueck, M., L. Nuijens, and B. Stevens, 2015: On the Seasonal and Synoptic Time-Scale Variability of the North Atlantic Trade Wind Region and Its Low-Level Clouds. *J. Atmospheric Sci.*, **72**, 1428–1446, https://doi.org/10.1175/JAS-D-14-0054.1.

Cao, L., G. Bala, and K. Caldeira, 2012: Climate response to changes in atmospheric carbon dioxide and solar irradiance on the time scale of days to weeks. *Environ. Res. Lett.*, **7**, 034015, https://doi.org/10.1088/1748-9326/7/3/034015.

Cesana, G. V., and A. D. Del Genio, 2021: Observational constraint on cloud feedbacks suggests moderate climate sensitivity. *Nat. Clim. Change*, **11**, 213–218, https://doi.org/10.1038/s41558-020-00970-y.

Chen, C., and W. R. Cotton, 1987: The Physics of the Marine Stratocumulus-Capped Mixed Layer. *J. Atmospheric Sci.*, **44**, 2951–2977, https://doi.org/10.1175/1520-0469(1987)044<2951:TPOTMS>2.0.CO;2.

Christensen, M. W., G. G. Carrió, G. L. Stephens, and W. R. Cotton, 2013: Radiative Impacts of Free-Tropospheric Clouds on the Properties of Marine Stratocumulus. *J. Atmospheric Sci.*, **70**, 3102–3118, https://doi.org/10.1175/JAS-D-12-0287.1.

De Roode, S. R., A. P. Siebesma, S. Dal Gesso, H. J. J. Jonker, J. Schalkwijk, and J. Sival, 2014: A mixed-layer model study of the stratocumulus response to changes in large-scale conditions. *J. Adv. Model. Earth Syst.*, **6**, 1256–1270, https://doi.org/10.1002/2014MS000347.

Eastman, R., and R. Wood, 2018: The Competing Effects of Stability and Humidity on Subtropical Stratocumulus Entrainment and Cloud Evolution from a Lagrangian Perspective. *J. Atmospheric Sci.*, **75**, 2563–2578, https://doi.org/10.1175/JAS-D-18-0030.1.

——, S. G. Warren, and C. J. Hahn, 2011: Variations in Cloud Cover and Cloud Types over the Ocean from Surface Observations, 1954–2008. *J. Clim.*, **24**, 5914–5934, https://doi.org/10.1175/2011JCLI3972.1.

Emanuel, K. A., 1991: A Scheme for Representing Cumulus Convection in Large-Scale Models. *J. Atmospheric Sci.*, **48**, 2313–2329, https://doi.org/10.1175/1520-0469(1991)048<2313:ASFRCC>2.0.CO;2.

Guan, H., M. K. Yau, and R. Davies, 1997: The Effects of Longwave Radiation in a Small Cumulus Cloud. *J. Atmospheric Sci.*, **54**, 2201–2214, https://doi.org/10.1175/1520-0469(1997)054<2201:TEOLRI>2.0.CO;2.

Hahn, C., and S. Warren, 2007: A Gridded Climatology of Clouds over Land (1971-1996) and Ocean (1954-2008) from Surface Observations Worldwide (NDP-026E)*. https://doi.org/10.3334/CDIAC/CLI.NDP026E.

Hartmann, D. L., M. E. Ockert-Bell, and M. L. Michelsen, 1992: The Effect of Cloud Type on Earth's Energy Balance: Global Analysis. *J. Clim.*, **5**, 1281–1304, https://doi.org/10.1175/1520-0442(1992)005<1281:TEOCTO>2.0.CO;2.

Jian, B., J. Li, L. Zhang, Y. Wang, W. Zhang, and Y. Li, 2022: Competition Between Radiative and Seeding Effects of Overlying Clouds on Underlying Marine

Stratocumulus. *Geophys. Res. Lett.*, **49**, https://doi.org/10.1029/2022GL100729.

Kamae, Y., and M. Watanabe, 2012: On the robustness of tropospheric adjustment in CMIP5 models: TROPOSPHERIC ADJUSTMENT IN CMIP5 MODELS. *Geophys. Res. Lett.*, **39**, n/a-n/a, https://doi.org/10.1029/2012GL054275.

——, and ——, 2013: Tropospheric adjustment to increasing CO_2: its timescale and the role of land–sea contrast. *Clim. Dyn.*, **41**, 3007–3024, https://doi.org/10.1007/s00382-012-1555-1.

Kato, S., and Coauthors, 2011: Improvements of top-of-atmosphere and surface irradiance computations with CALIPSO-, CloudSat-, and MODIS-derived cloud and aerosol properties. *J. Geophys. Res.*, **116**, D19209, https://doi.org/10.1029/2011JD016050.

Klein, S. A., and D. L. Hartmann, 1993: The Seasonal Cycle of Low Stratiform Clouds. *J. Clim.*, **6**, 1587–1606, https://doi.org/10.1175/1520-0442(1993)006<1587:TSCOLS>2.0.CO;2.

——, A. Hall, J. R. Norris, and R. Pincus, 2017: Low-Cloud Feedbacks from Cloud-Controlling Factors: A Review. *Surv. Geophys.*, **38**, 1307–1329, https://doi.org/10.1007/s10712-017-9433-3.

Klinger, C., B. Mayer, F. Jakub, T. Zinner, S.-B. Park, and P. Gentine, 2017: Effects of 3-D thermal radiation on the development of a shallow cumulus cloud field. *Atmospheric Chem. Phys.*, **17**, 5477–5500, https://doi.org/10.5194/acp-17-5477-2017.

Lilly, D. K., 1968: Models of cloud-topped mixed layers under a strong inversion. *Q. J. R. Meteorol. Soc.*, **94**, 292–309, https://doi.org/10.1002/qj.49709440106.

Malkus, J. S., 1954: SOME RESULTS OF A TRADE-CUMULUS CLOUD INVESTIGATION. *J. Meteorol.*, **11**, 220–237, https://doi.org/10.1175/1520-0469(1954)011<0220:SROATC>2.0.CO;2.

Minnis, P., and Coauthors, 2011: CERES Edition-2 Cloud Property Retrievals Using TRMM VIRS and Terra and Aqua MODIS Data—Part II: Examples of Average Results and Comparisons With Other Data. *IEEE Trans. Geosci. Remote Sens.*, **49**, 4401–4430, https://doi.org/10.1109/TGRS.2011.2144602.

Muhlbauer, A., I. L. McCoy, and R. Wood, 2014: Climatology of stratocumulus cloud morphologies: microphysical properties and radiative effects. *Atmospheric Chem. Phys.*, **14**, 6695–6716, https://doi.org/10.5194/acp-14-6695-2014.

Myers, T. A., and J. R. Norris, 2013: Observational Evidence That Enhanced Subsidence Reduces Subtropical Marine Boundary Layer Cloudiness. *J. Clim.*, **26**, 7507–7524, https://doi.org/10.1175/JCLI-D-12-00736.1.

——, and ——, 2016: Reducing the uncertainty in subtropical cloud feedback. *Geophys. Res. Lett.*, **43**, 2144–2148, https://doi.org/10.1002/2015GL067416.

Norris, J. R., 1998: Low Cloud Type over the Ocean from Surface Observations. Part II: Geographical and Seasonal Variations. *J. Clim.*, **11**, 383–403, https://doi.org/10.1175/1520-0442(1998)011<0383:LCTOTO>2.0.CO;2.

——, and S. A. Klein, 2000: Low Cloud Type over the Ocean from Surface Observations. Part III: Relationship to Vertical Motion and the Regional Surface Synoptic Environment. *J. Clim.*, **13**, 245–256, https://doi.org/10.1175/1520-0442(2000)013<0245:LCTOTO>2.0.CO;2.

——, R. J. Allen, A. T. Evan, M. D. Zelinka, C. W. O'Dell, and S. A. Klein, 2016: Evidence for climate change in the satellite cloud record. *Nature*, **536**, 72–75, https://doi.org/10.1038/nature18273.

Qu, X., A. Hall, S. A. Klein, and P. M. Caldwell, 2014: On the spread of changes in marine low cloud cover in climate model simulations of the 21st century. *Clim. Dyn.*, **42**, 2603–2626, https://doi.org/10.1007/s00382-013-1945-z.

Schneider, S. H., 1972: Cloudiness as a Global Climatic Feedback Mechanism: The Effects on the Radiation Balance and Surface Temperature of Variations in Cloudiness. *J. Atmospheric Sci.*, **29**, 1413–1422, https://doi.org/10.1175/1520-0469(1972)029<1413:CAAGCF>2.0.CO;2.

Schneider, T., C. M. Kaul, and K. G. Pressel, 2019: Possible climate transitions from breakup of stratocumulus decks under greenhouse warming. *Nat. Geosci.*, **12**, 163–167, https://doi.org/10.1038/s41561-019-0310-1.

Scott, R. C., T. A. Myers, J. R. Norris, M. D. Zelinka, S. A. Klein, M. Sun, and D. R. Doelling, 2020: Observed Sensitivity of Low-Cloud Radiative Effects to Meteorological Perturbations over the Global Oceans. *J. Clim.*, **33**, 7717–7734, https://doi.org/10.1175/JCLI-D-19-1028.1.

Slingo, A., 1990: Sensitivity of the Earth's radiation budget to changes in low clouds. *Nature*, **343**, 49–51, https://doi.org/10.1038/343049a0.

Stevens, B., and J.-L. Brenguier, 2009: Cloud-controlling Factors: Low Clouds. *Clouds in the Perturbed Climate System*, J. Heintzenberg and R.J. Charlson, Eds., The MIT Press, 173–196.

Stommel, H., 1947: ENTRAINMENT OF AIR INTO A CUMULUS CLOUD: (Paper presented 27 December 1946 at the Annual Meeting, A.M.S., Cambridge, Massachusetts). *J. Meteorol.*, **4**, 91–94, https://doi.org/10.1175/1520-0469(1947)004<0091:EOAIAC>2.0.CO;2.

Sun, M., D. R. Doelling, N. G. Loeb, R. C. Scott, J. Wilkins, L. T. Nguyen, and P. Mlynczak, 2022: Clouds and the Earth's Radiant Energy System (CERES) FluxByCldTyp Edition 4 Data Product. *J. Atmospheric Ocean. Technol.*, **39**, 303–318, https://doi.org/10.1175/JTECH-D-21-0029.1.

Van Der Dussen, J. J., S. R. De Roode, S. Dal Gesso, and A. P. Siebesma, 2015: An LES model study of the influence of the free tropospheric thermodynamic conditions on the stratocumulus response to a climate perturbation: Influence of free troposphere on SCu. *J. Adv. Model. Earth Syst.*, **7**, 670–691, https://doi.org/10.1002/2014MS000380.

Warren, S., C. Hahn, J. London, R. Chervin, and R. Jenne, 1988: *Global Distribution of Total Cloud Cover and Cloud Type Amounts Over the Ocean*. UCAR/NCAR,.

Wielicki, B. A., B. R. Barkstrom, E. F. Harrison, R. B. Lee, G. Louis Smith, and J. E. Cooper, 1996: Clouds and the Earth's Radiant Energy System (CERES): An Earth Observing System Experiment. *Bull. Am. Meteorol. Soc.*, **77**, 853–868, https://doi.org/10.1175/1520-0477(1996)077<0853:CATERE>2.0.CO;2.

Wood, R., 2012: Stratocumulus Clouds. *Mon. Weather Rev.*, **140**, 2373–2423, https://doi.org/10.1175/MWR-D-11-00121.1.

——, and C. S. Bretherton, 2006: On the Relationship between Stratiform Low Cloud Cover and Lower-Tropospheric Stability. *J. Clim.*, **19**, 6425–6432, https://doi.org/10.1175/JCLI3988.1.

Zelinka, M. D., S. A. Klein, and D. L. Hartmann, 2012: Computing and Partitioning Cloud Feedbacks Using Cloud Property Histograms. Part II: Attribution to Changes in Cloud Amount, Altitude, and Optical Depth. *J. Clim.*, **25**, 3736–3754, https://doi.org/10.1175/JCLI-D-11-00249.1.

——, ——, K. E. Taylor, T. Andrews, M. J. Webb, J. M. Gregory, and P. M. Forster, 2013: Contributions of Different Cloud Types to Feedbacks and Rapid Adjustments in CMIP5*. *J. Clim.*, **26**, 5007–5027, https://doi.org/10.1175/JCLI-D-12-00555.1.

Zhang, M., and Y. Huang, 2014: Radiative Forcing of Quadrupling CO_2. *J. Clim.*, **27**, 2496–2508, https://doi.org/10.1175/JCLI-D-13-00535.1.